이 학 석 사 학 위 논 문

Synthesis of New Porous Metal-Organic Frameworks and Studies on Application in Carbon Dioxide Capture

새로운 다공성 금속-유기 골격체의 합성과 이산화탄소 포집에의 응용연구

2013 년 8 월

서울대학교 대학원

화학부 무기화학 전공

최 명 호

Synthesis of New Porous Metal-Organic Frameworks and Studies on Application in Carbon Dioxide Capture

새로운 다공성 금속-유기 골격체의 합성과 이산화탄소 포집에의 응용연구

지도교수 백 명 현

이 논문을 이학석사 학위논문으로 제출함

2013 년 8 월

서울대학교 대학원

화학부 무기화학 전공

최 명 호

최 명 호의 이학석사 학위논문을 인준함

2013 년 8 월

위 원 장 _____ (인)

부 위 원 장 _____ (인)

위 원 _____ (인)

Synthesis of New Porous Metal-Organic Frameworks and Studies on Application in Gas molecule Capture

By

Myung-Ho Choi

Supervisor: Prof. Myunghyun Paik Suh

A Thesis for the M.S. Degree

In Inorganic Chemistry

Department of Chemistry

Graduate School

Seoul National University

August, 2013

Table of contents

Abstract

Two porous MOFs, $[Zn_4O(NTN)_2]\cdot 11DMA\cdot 2H_2O$ (**SNU-150**) (**(**H_3NTN= 6,6',6''-nitrilotri-2-naphthoic acid, (DMA = *N*,*N*-dimethylacetamide) and $[Zn_5(NTN)_4(DEF)_2][NH_2(C_2H_5)_2]_2\cdot 8DEF\cdot 6H_2O$ (**SNU-151**) (DEF = *N*,*N*-diethylformamide) have been synthesized by using the same metal and organic building blocks but in the different solvent systems, in DMA and in the mixture of DEF and acetic acid, respectively. The framework of **SNU-150** is neutral whereas **SNU-151** is an anionic framework including diethyl ammonium cations as guests. Whether or not a small amount of acetic acid is added in the reaction mixture gives rise to totally different framework structures, since the acid hydrolyzes DEF solvent to produce diethyl ammonium cations that should be included in the cavities of the MOF. Desolvated solids $[Zn_4O(NTN)_2]$ (**SNU-150'**) and $[Zn_5(NTN)_4][NH_2(C_2H_5)_2]_2$ (**SNU-151'**), respectively, were obtained by treatment of **SNU-150** and **SNU-151** with supercritical CO_2. **SNU-151'** exhibits higher H_2, CO_2, and CH_4 gas adsorption capacities than **SNU-150'**, due to the stronger interaction of the gas molecules with the anionic framework and ammonium cations included in the channels, compared to that with neutral **SNU-150'**.

keywords **: Porous metal-organic frameworks, CO_2 capture, anionic frameworks, adsorption heat, selectivity**

1. Introduction

Carbon dioxide (CO_2) emissions have become one of the most serious issues and environmental concerns facing our civilization today.[1] These emissions are mainly generated from industrialized communities which emitted flue gas. Because the flue gas is main attributor of global greenhouse effect which threats our unimpaired life, before we realize the cleaner alternative energy and establish the energy infrastructure for the implementation of new materials and technologies in the future, minimizing of emitted CO_2 gas to the atmosphere is very important issue.

Porous metal-organic frameworks (MOFs) with well-defined channels or pores have attracted great attention because of their potentials in application to hydrogen storage,[2-5] carbon dioxide separation, capture,[6-9] ion exchange[10, 11], drug delivery[12, 13], and catalytic activity[14]. In particular, selective and reversible capture of carbon dioxide from industrial flue gas which is major attributor global greenhouse effect has become one of the most important issues recently in the scientific community. Industrial flue gas contains 15% of CO_2, 75% of N_2, and other minor components. The CO_2 gas emitted from the combustion of carbon-based fossil fuels, which is major source of greenhouse effect.[15] To apply a MOF in capturing CO_2 from industrial flue gas its storage capacity at ambient temperatures under low pressure (0.15 atm) of CO_2 and adsorption selectivity for CO_2 over other gases should be high. The gas adsorption capacities of MOFs are affected by the surface areas, presence of accessible metal sites (AMSs), and functional groups. The ions or molecules included in the pores of the MOFs also affect selective gas sorption ability. The design of MOFs as functional materials for selective gas adsorbent can be

achieved by choosing proper metal sources, organic building blocks and solvent system.

In this introduction, synthesis of porous metal-organic frameworks and their functionalization and properties which can enhance interaction between MOFs and gas molecules.

1. 1. Porous Metal-Organic Frameworks

Porous metal-organic frameworks are a new class of solids that have attracted much recent attention owing to their potential applications in a variety of areas, including hydrogen storage,[2-5] carbon dioxide separation, capture,[6-9] ion exchange[10, 11], drug delivery[12, 13], and catalytic activity[14]. These structures consist of metal-based nodes (metal ions or clusters) bridged by organic linkers to form a one-, two-, or three-dimensional coordination network. From an applications point of view, their especially high surface areas[16], easily tunable pore surface properties[17] have made these materials an attractive target for further study.

1. 2. Synthesis and Structural features

The synthesis of metal-organic frameworks is achieved by employing metal ions and organic linkers are combined to afford a crystalline, porous network. Exceedingly variety of synthetic methods have been developed in recent years for the preparation of these materials, and the conditions, reactant ratio and concentration, solvent system, and use of a secondary ligand[18] that lead to the formation of the desired phases are widely variable. The proper preparation of all of these parameters has crucial role in optimizing the synthesis of the materials.

In the context of CO_2 capture, the surfaces of MOFs can be utilized to perform the gas adsorption and separation. One of the most well-studied metal-organic frameworks is the $Zn_4O(BDC)_3$ (MOF-5) (BDC : benzene dicarboxylate) compound depicted in Figure 1,[19-21] which consists of tetrahedral $[Zn_4O]^{6+}$ clusters bridged by BDC^{2-} ligands to form a cubic, 3 D network.

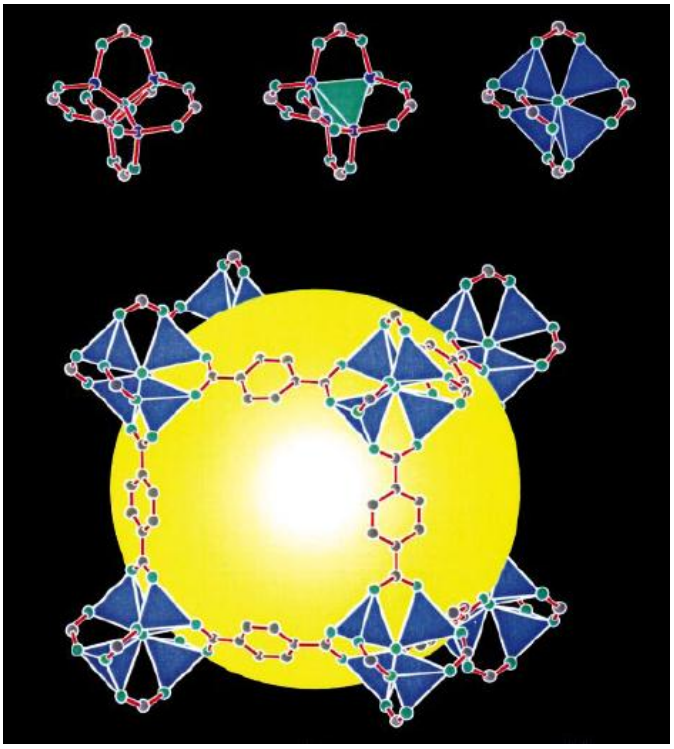

Figure 1. Construction of the MOF-5 framework. Top, the $Zn_4(O)O_{12}C_6$ cluster. Left, as a ball and stick model (Zn, blue; O, green; C, grey). Middle, the same with the $Zn_4(O)$ tetrahedron indicated in green. Right, the same but now with the Zn_4O tetrahedra indicated in blue. Bottom, one of the cavities in the $Zn_4(O)(BDC)_3$, MOF-5 framework. Eight clusters (only seven visible) constitute a unit cell and enclose a large cavity, indicated by a yellow sphere of diameter 18.5 Å in contact with 72 C atoms (grey).[19]

Importantly, functionalized derivatives of the MOF-5 structure type can be prepared using other functionalized linear dicarboxylate linkers, allowing the linker length or functional groups present on the aromatic backbone to be readily modified, while preserving the overall structure and connectivity of the framework.[22, 23] This family of materials, so-called isoreticular Metal-organic frameworks (IRMOFs), feature considerably different pore sizes and pore characteristics, suggesting that the properties of the materials can be finely tuned by employing the appropriate linker type.

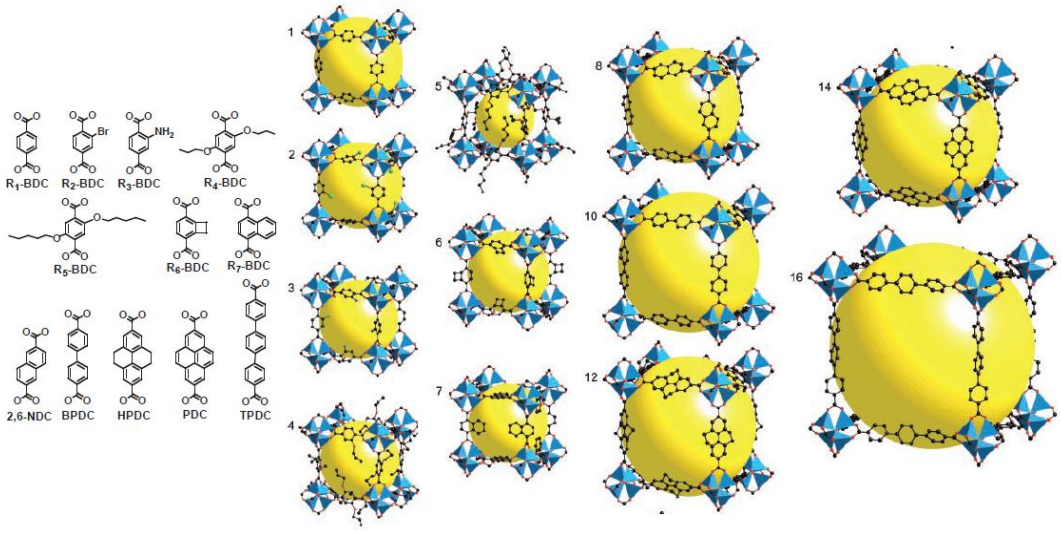

Figure. 2 Single crystal x-ray structures of IRMOF-n (n=1 through 7, 8, 10, 12, 14, and 16), labeled respectively. The doubly interpenetrated IRMOFs (9, 11, 13, and 15) are not shown. Color scheme is as follows: Zn (blue polyhedra), O (red spheres), C (black spheres), Br (green spheres in 2), amino-groups (blue spheres in 3). The large yellow spheres represent the largest van der Waals spheres that would fit in the cavities without touching the frameworks. All hydrogen atoms have been omitted, and only one orientation of disordered atoms is shown for clarity.[23]

Yaghi and co-workers synthesized 18 multivariate (MTV) MOF-5 structures by combining the acid form of 1,4-benzenedicarboxylate (BDC), NH_2-BDC, Br-BDC, $(Cl)_2$-BDC, NO_2-BDC, $(CH_3)_2$-BDC, C_4H_4-BDC, $(OC_3H_5)_2$-BDC, and (OC_7H_7)BDC links (Figure 3, A to I, respectively). Each MTV-MOF-5 has two to eight different functionalities in the same structure as MOF-5, as evidenced by powder X-ray diffraction (PXRD), 13C cross-polarization/magic angle spinning nuclear magnetic resonance (13C CP/MAS NMR), and 1H NMR on acid-digested solutions of their crystals. The complex arrangements of several functional groups within the pores can lead to properties that are not simply linear combinations of those of the pure components. In particular, MTV-MOF-5-EHI, exhibits the fourfold enhancement of selectivity for carbon dioxide over carbon monoxide compared with MOF-5. These finding demonstrate that the sequence of functionalities within the MOF might be very useful for the enhancement of a specific property or achieving a new property.[24]

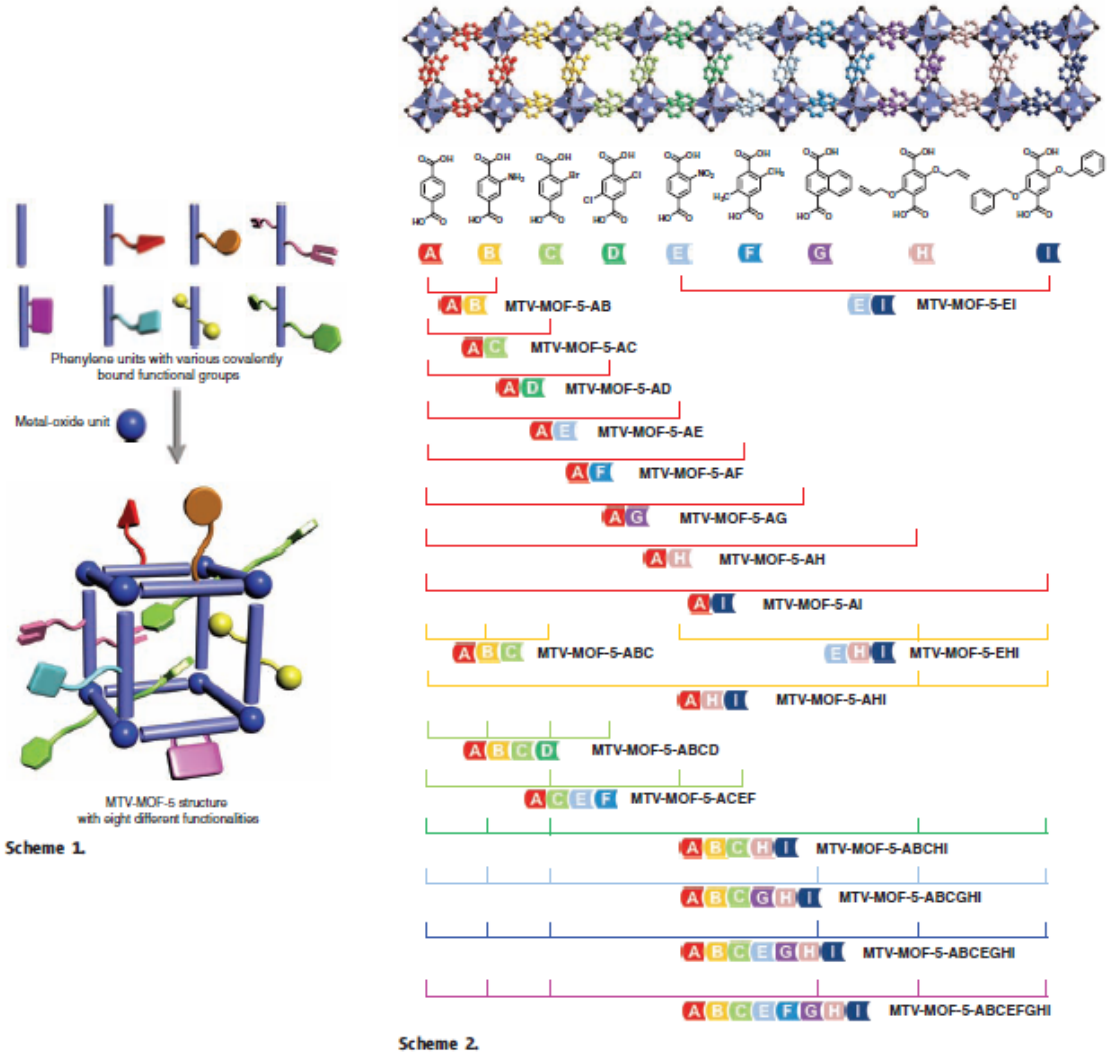

Figure 3. Schemes of 18 MTV-MOF-5.[24]

In CO_2 capture point, the ability to readily modify the surface of MOFs is of particular interest for installing the desired chemical features (such as amines or polarizing groups) for enhancing the performance of the material.

1. 2. 1. Post-Synthetic Modification

An important path to construct the desired functionalities on the organic bridge is the post-synthetic modification of the surface functional groups following the initial formation of the metal-organic frameworks.[25, 26] One advantage of such an approach is that functional groups that might interfere with the formation of the framework owing to their propensity to bind metal ions (such as amines, alcohols, and aldehydes) can be installed with well-known organic transformations once the framework scaffold has been formed, eliminating the need to develop precise reaction conditions to form the material directly. Such a procedure has been demonstrated on compounds such as IRMOF-3,[27] DMOF-1-NH2,[28, 29] UiO-66-Br,[30] and MIL-101(Cr),[31] and the scope of reactions available is growing rapidly.

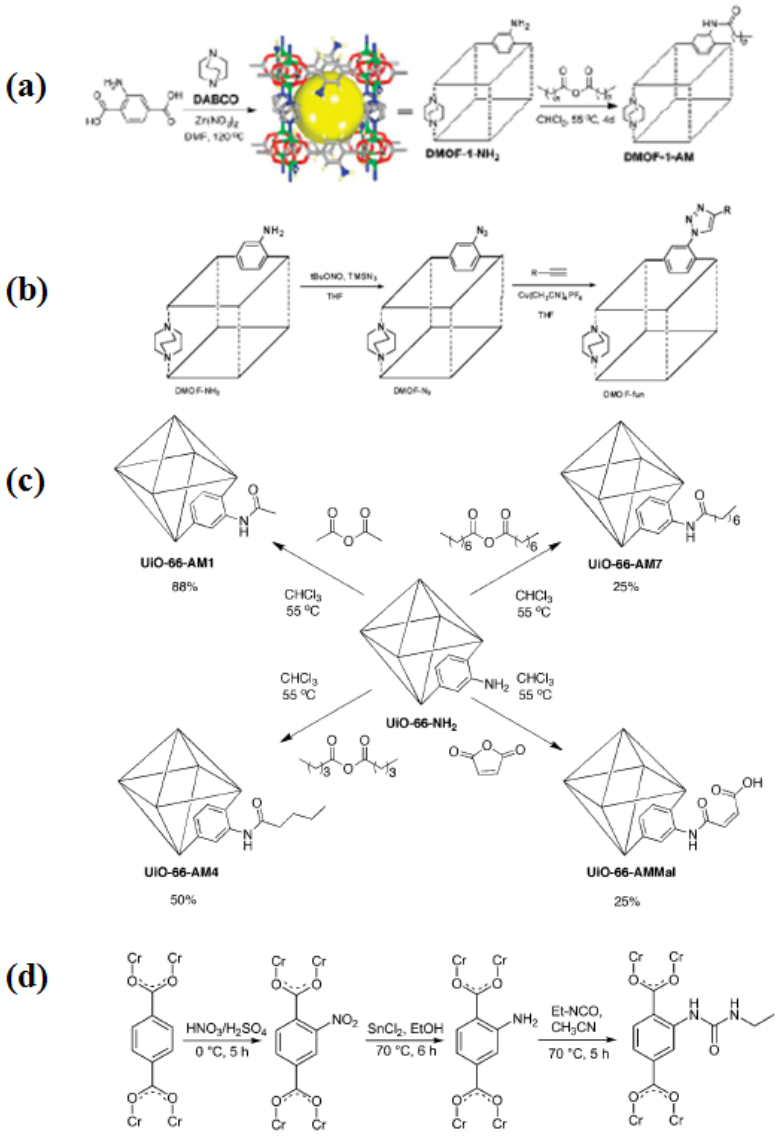

Figure 4. Post-synthetic modification schemes. a) DMOF-1-NH_2 with Linear Alkyl Anhydrides,[28] b) One-Pot, Two-Step functionalization of DMOF-NH_2,[29] c) UiO-66–NH_2 with various anhydrides,[30] d) Nitration of Cr-MIL-101 leads to Cr-MIL-101–NO_2 which was reduced to Cr-MIL-101–NH_2 and further reacted with ethyl isocyanate to yield the urea derivative Cr-MIL-101–UR2.[31]

1. 2. 2. Accessible metal sites (AMSs)

There is an alternative strategy of preparing metal-organic frameworks with functionalized surfaces is the generation of accessible metal centers (AMSs).[32-36] The AMSs can facilitate highly selective interactions with certain gas molecules in separation and gas storage applications. There is one of the materials which are intensively studied featuring such binding sites is $Cu_3(BTC)_2$ (HKUST-1), which exhibits a cubic, twisted boracite topology constructed from Cu^{2+} paddlewheel type of secondary building units (SBUs) and triangular 1,3,5-

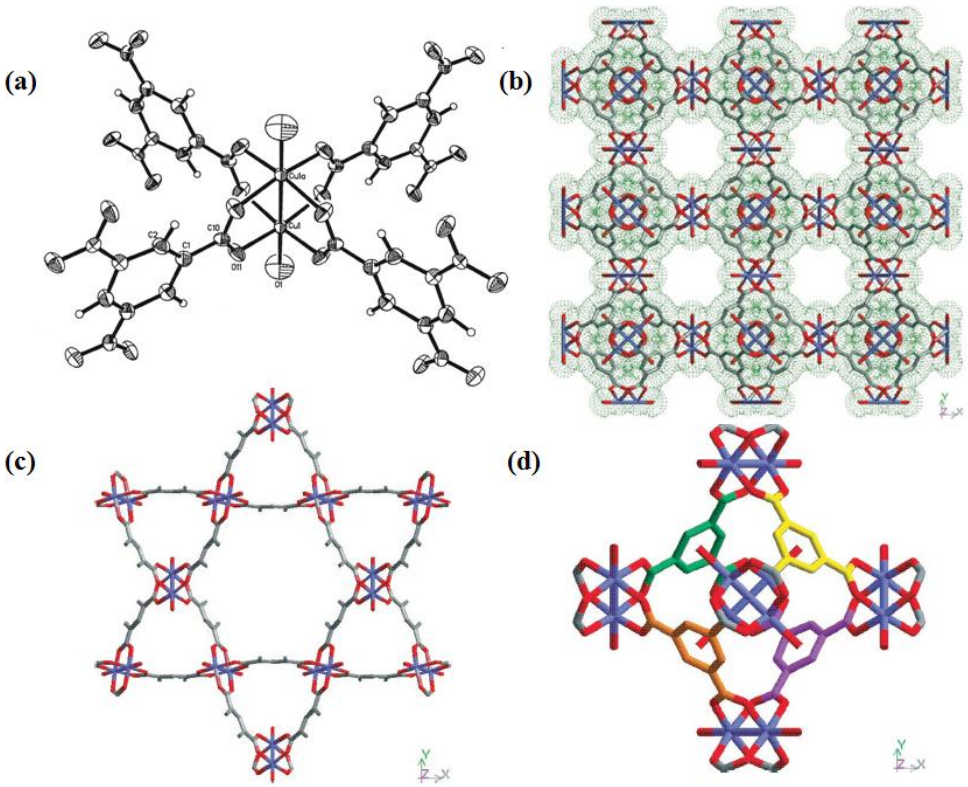

Figure 5. crystal structure of $Cu_3(BTC)_2$ (HKUST-1).[37] a) Dicopper(II) tetracarboxylate building block for HKUST-1, b) HKUST-1 polymer framework viewed down the [100]

direction, showing nanochannels with fourfold symmetry, c) HKUST-1 viewed along the cell body diagonal [111], showing a hexagonalshaped 18 Å window at the intersection of the nanopores, d) Secondary building unit for $[Cu_3(BTC)_2(H_2O)_3]n$, viewed along the [100] direction. The Cu_2 dimers bridge to other such SBUs.

benzenetricarboxylate linkers (see Figure 5).[37] The as-synthesized form of the HKUST-1 contains bound solvent molecules on the axial coordination sites of each Cu^{2+} metal center in SBU, which can be subsequently removed by heat evacuation to create accessible metal sites (AMSs) for guest molecules. Indeed, these sites act as charge-dense point charges, which provide an opportunity for discrimination of certain components of gas mixtures based on their polarizability and dipole or quadrupole moment. The adsorptive properties of MOFs which have AMSs can be dramatically tuned based on the charge density present at the metal coordination site. Wu and coworker studied the binding sites of CO_2 on two MOFs, Mg-MOF-74 and HKUST-1, through neutron diffraction measurements.[38] Both Mg-MOF-74 and HKUST-1 have AMSs and neutron diffraction studies showed that AMSs are the major contributor of CO_2 adsorption (Figure. 6).

In both MOFs, the strongest binding performance between AMSs and CO_2 are attributed to enhanced electrostatic interaction. In Mg-MOF-74, all CO_2 molecules bind to the bared Mg^{2+} site. In the case of HKUST-1, most CO_2 molecules bind to the bared Cu^{2+} sites at low CO_2 concentration, and large amounts of CO_2 go into the small cage window only at high loading.

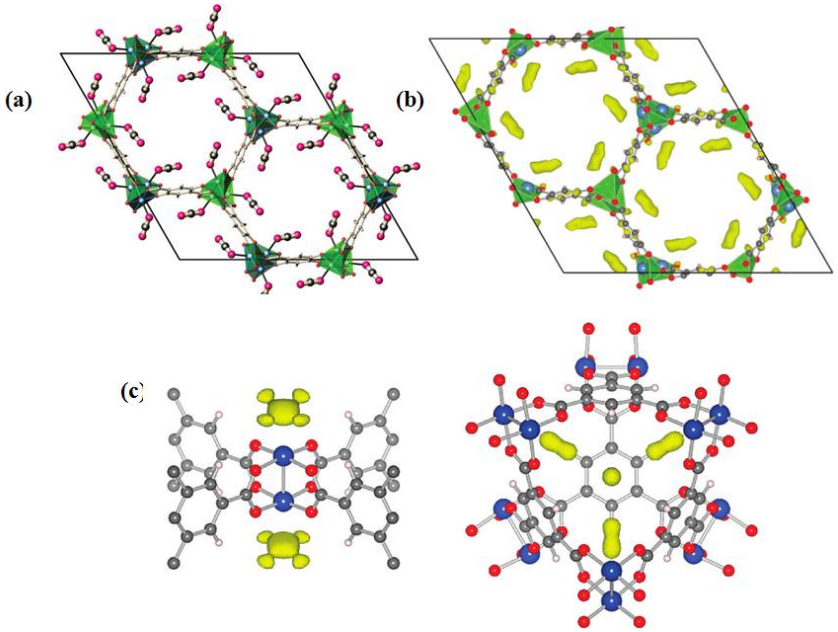

Figure 6. a) CO_2 binding on Mg-MOF-74. b) Real space Fourier difference scattering length density (yellow regions) superimposed on the Mg-MOF-74 structure (color scheme of atoms: Mg, blue; C, gray; O, red; and H, white), clearly indicating that the adsorbed CO_2 is located on top of the open Mg ions. c) Real space Fourier difference scattering length density (yellow regions) superimposed with the partial structure of HKUST-1 (color scheme of atoms: Cu, blue; C, gray; O, red; and H, white), clearly indicating that the adsorbed CO_2 is primarily located on top of the open Cu ions (left) and the window opening of the small octahedral cage (right).[38]

For adsorption sites other than AMSs, van der Waals interaction holds the adjacent CO_2 molecules. Accessible small cages and channels often provide relatively stronger van der Waals interaction since the gas molecules can interact with multiple 'surfaces'.[39] The HKUST-1 is a good example for presenting CO_2 adsorption in the small cage window

sites. The adsorbed CO_2 vibrational mode based on first-principles calculations reveals that CO_2 molecules are attached to the metal sites with one of its oxygen atoms and the rest of the molecule is relatively free. Calculations also indicated the CO_2-metal interaction is still physisorptive and the MOFs can be regenerated. The study demonstrates that AMSs is one of the most important features to consider in the development of new MOFs for CO_2 capture materials.

Suh's group report two porous MOFs with the same NbO type net topology, and compare the gas adsorption data for the MOFs with and without AMSs.[40] The MOFs $[\{Zn_2(abtc)(dmf)_2\}_3]$ (abtc : 1,1'-azobenzene3,3',5,5'-tetracarboxylate, dmf : dimethylformamide) (SNU-4), $[\{Cu_2(abtc)(dmf)_2\}_3]$ (SNU-5'), which have no AMSs, and $[\{Cu_2(abtc)\}_3]$ (SNU-5), which has AMSs, where prepared by solvothermal reaction and subsequently heat evacuation. The combination between metal paddle-wheel secondary building unit and planar tetracarboxylate generate 3 D NbO type network structure (Figure. 7).

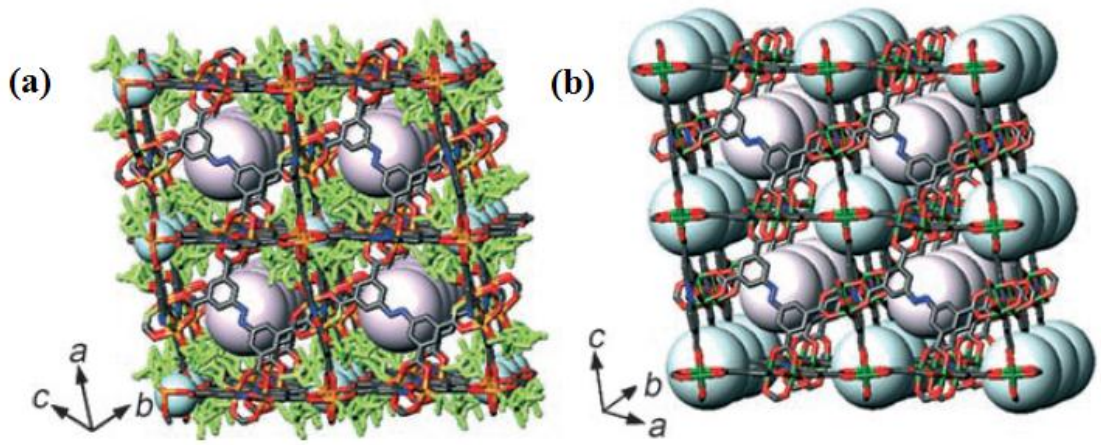

Figure 7. X-ray crystal structures of a) $[\{Zn_2(abtc)(dmf)_2\}_3]\cdot 4H_2O\cdot 10dmf$ and b) $[\{Cu_2(abtc)(H_2O)_2\}_3]\cdot 10$ dmf·6 (1,4-dioxane) showing their NbO type 3D frameworks. The two kinds of spheres (in light blue and gray) represent the open spaces that can be occupied by the guest molecules without touching the framework. Hydrogen atoms and guest molecules have been omitted for clarity. The coordinated water molecules in 2 have also been omitted. Color scheme: Zn orange, Cu green, C gray, O red, N blue, coordinated dmf yellowish green.[40]

In SNU-4 and SNU-5', the networks have a coordinating DMF molecules in the axial sites of paddle-wheel units, while, in SNU-5, the coordinated water molecules in axial site of paddle wheel unit is lost, which resulted in AMSs. The surface area, pore volume, H_2 uptake amount, and adsorption heat for H_2 are shown in Table 1. The MOF with AMSs clearly has a higher H_2 adsorption in terms of wt% compared to those with no AMSs.

Table 1.

	Surface area	Pore volume	H_2 uptake amount (wt% at 77 K)	Adsorption heat
SNU-4	1460 m^2g^{-1} (1491 m^2g^{-1})	0.53 cm^3g^{-1} (0.54 cm^3g^{-1})	2.07 3.70[a] 4.49[b]	5.96-7.24 kJ mol^{-1} kJ mol^{-1}
SNU-5	1260 m^2g^{-1} (1261 m^2g^{-1})	0.48 cm^3g^{-1} (0.48 cm^3g^{-1})	1.83	5.91-6.53 kJ mol^{-1}
SNU-5’	2850 m^2g^{-1} (2189 m^2g^{-1})	1.00 cm^3g^{-1} (0.77 cm^3g^{-1})	2.87 5.22[a] 6.76[b]	4.43-11.60 kJ mol^{-1}

[a] Excess adsorption capacity at 77 K and 50 bar. [b] Total adsorption capacity at 77 K and 50 bar.

1. 2. 3. Charged frameworks

One of the key parameters has to be tuned to improve the interaction energies of gas molecules provided by charged metal-organic frameworks. The introduction of electrostatic field in the cavities and channels by having a charged framework, along with extra-framework cations, can strengthen interaction energy between host and gas molecules. In charged framework case, additionally metal ion exchange could enhance adsorption heat also. Suh’s group demonstrate by experimental and theoretical studies that the impregnation of various metal ions such as Li^+, Mg^{2+}, Ca^{2+}, Co^{2+}, and Ni^{2+} in the pores of an anionic MOF, $[Zn_3(TCPT)_2(HCOO)][NH_2(CH_3)_2]$ (**SNU-100**) significantly enhances isosteric heat, selectivity, and uptake capacity of the CO_2 adsorption in the

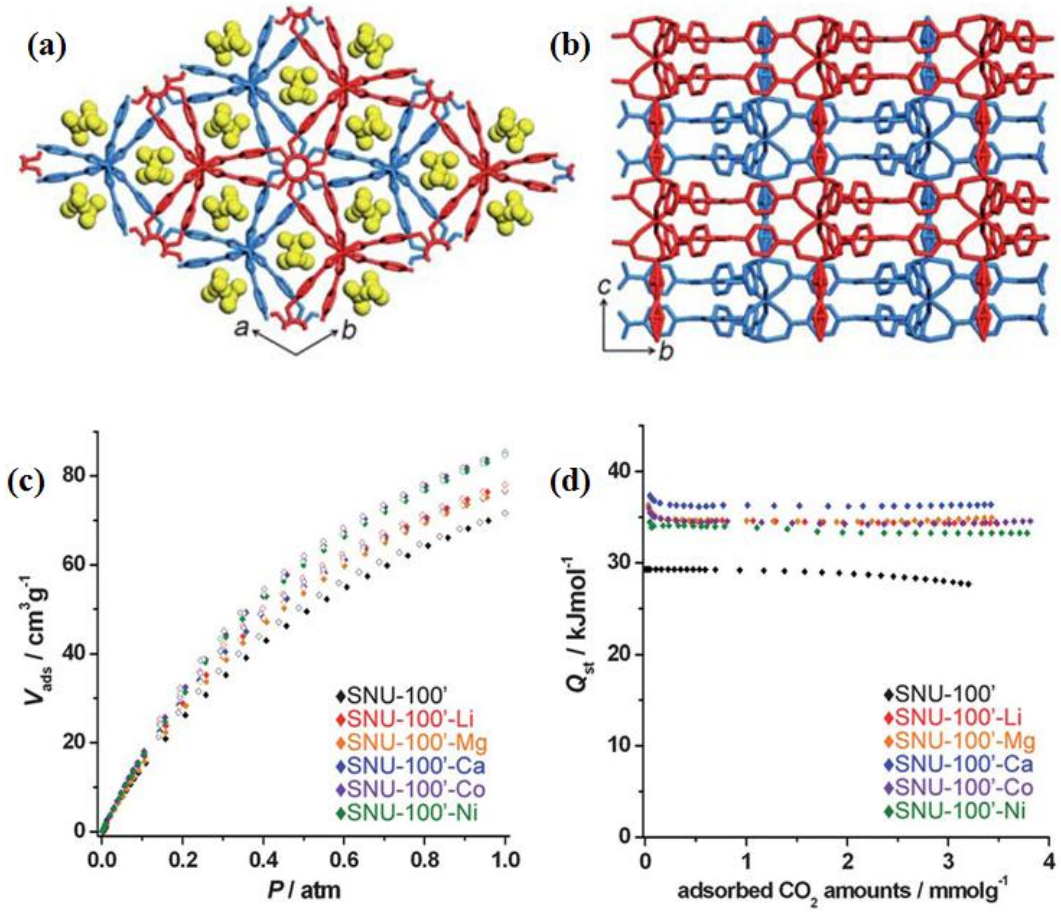

Figure 8. a) X-Ray crystal structure of **SNU-100**' seen on the ab plane. b) View seen on the bc plane. Doubly interpenetrated anionic frameworks are represented in two different colors (red and blue) and $[NH_2(CH_3)_2]^+$ cations refined are represented in yellow. c) (a) CO_2 sorption isotherms of **SNU-100-M** at 298 K. Filled shapes: adsorption. Open shapes: desorption. d) Adsorption heat of CO_2 adsorption. (**SNU-100-M** : metal cation exchanged **SNU-100**).[41]

MOF.[41] Due to the electrostatic interactions between CO_2 and the extra-framework metal

ions, the isosteric heats of CO_2 adsorption are increased to 37.4–34.5 kJ mol^{-1} and the adsorption selectivities of CO_2 over N_2 at room temperature are increased to 40.4–31.0, compared with those (29.3 kJ mol^{-1} and 25.5 kJ mol^{-1}, respectively) of the parent MOF (SNU-100) containing $[NH_2(CH_3)_2]^+$ cations.

1. 3. Activation methods

Many potential applications of MOFs take advantage of the especially high surface areas offered by this emerging class of tunable materials. Typically as-synthesized MOFs have solvent molecules in the pores and channels. The low boiling point solvent can be easily eliminated by evacuation at elevated temperature, and activated MOFs exhibit surface areas that are only a small fraction of what is predicted based on their structure. This problem becomes even more severe for MOFs that keep high boiling point solvents in the pores and channels. In this case, exchanging high boiling point solvent and lower boiling point solvent could be good approach to activate MOFs. There, however are some cases that could be destructed frameworks and lost crystallinity by exchanging solvent system.

Hupp's group reported, the surface areas of Zinc MOFs, can be significantly increased by supercritical carbon dioxide processing, presumably by preventing the mesopore collapse and thus enhancing micropore accessibility as a result of the low surface tension of supercritical carbon dioxide.[42]

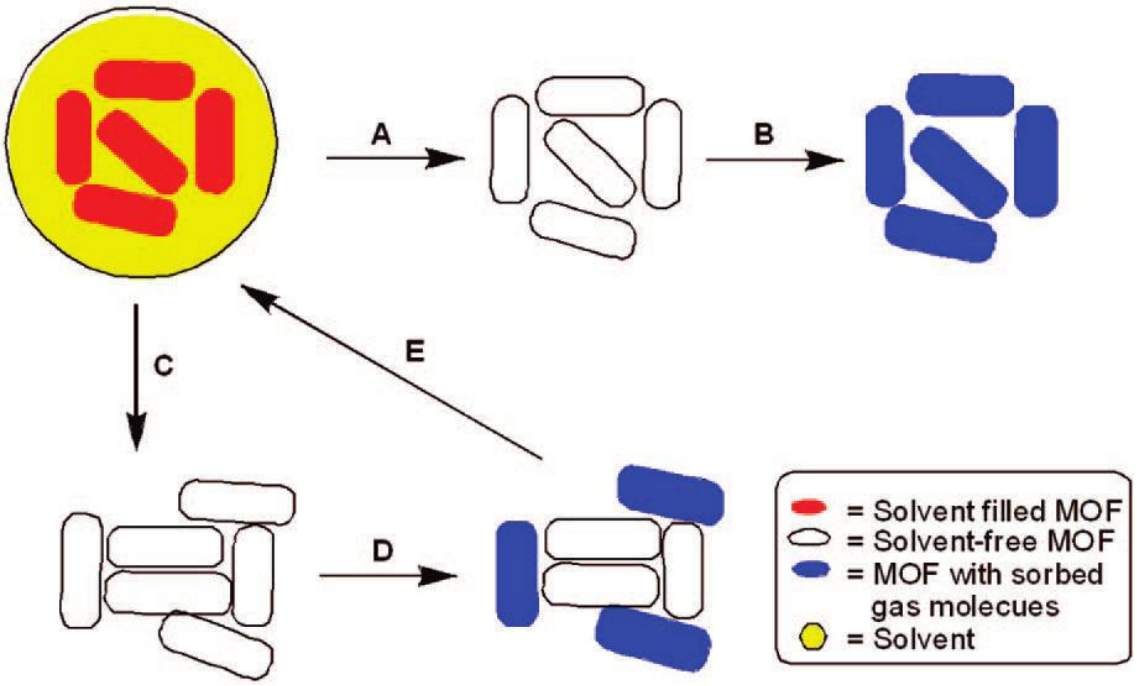

Figure 9. a) Supercritical CO2 activation of MOF microcrystals, (b) adsorption of gas molecules after supercritical CO2 activation, (c) traditional activation of MOF crystals, (d) adsorption of gas molecules after traditional activation, and (e) resolvation.[42]

1. 4. Adsorption Heat of CO_2 and Selectivity for CO_2 over Other Gases

The thermodynamic definition of the adsorption heat of a pure gas is the molar enthalpy in the adsorbed phase.

$$Q_{st} = h^g - \left[\frac{\partial H^m}{\partial n^m}\right]_T \qquad \textit{(Eq. 1)}$$

where H^m is the specific enthalpy [J/kg] of the adsorbed phase and n^m is the specific amount adsorbed [mol/kg].[43] The m superscript denotes that the variables are measured Gibbs excess variables; absolute values calculated by molecular simulation must be converted to excess variables for comparison with experiment. For a real gas, the isothermal variation of its enthalpy with pressure introduces residual enthalpy nuisance terms into the thermodynamic equations. Since our experiments are performed at sub-atmospheric pressure, the following equations are written for the case when the bulk gas obeys the perfect gas law. It can then be shown that (*Eq. 1*) is equivalent to:

$$Q_{st} = -R\left[\frac{\partial \ln P}{\partial (1/T)}\right]_{n^m} \qquad \textit{(Eq. 2)}$$

Plots of *lnP* as a function of reciprocal absolute temperature at constant loading are called adsorption isosteres; *(Eq. 2)* shows that the adsorption heat is determined by their slope.

The adsorption heat of gas adsorption is usually evaluated by fitting the CO_2 adsorption isotherm measured at two or more independent temperatures to following Langmuir-type equations *(Eq. 3)*.

$$\frac{N}{N_{sat}} = \frac{bP}{1+bP} \qquad \textit{(Eq. 3)}$$

$$\frac{N}{N_{sat}} = \frac{bP^{1/t}}{1+bP^{1/t}} \qquad \textit{(Eq. 4)}$$

$$\frac{N}{N_{sat}} = \frac{bP}{(1+bP^t)^{1/t}} \qquad \textit{(Eq. 5)}$$

$$N = \frac{N_{sat,A} b_A P}{1+b_A P} + \frac{N_{sat,B} b_B P}{1+b_B P} \qquad \textit{(Eq. 6)}$$

$$N = \frac{N_{sat,A} b_A P^{\alpha_A}}{1+b_A P^{\alpha_A}} + \frac{N_{sat,B} b_B P^{\alpha_B}}{1+b_B P^{\alpha_B}} \qquad \textit{(Eq. 7)}$$

Where N is amount of adsorbed gas, N_{sat} is amount of adsorbed gas at saturation, P is pressure, and b and t are the constants. *(Eq. 4)* is Langmuir-Freundlich equation and *(Eq. 5)* is Toth equation.

A dual-site Langmuir equation *(Eq. 6)* and dual-site Langmuir-Freundlich equation *(Eq. 7)* are also employed to model the gas adsorption. These equations are given by the sum of two single-site Langmuir equations and suitable for describing systems where the interactions between the gas and the host adsorbent are complicated and more than one kind of adsorption sites exist with different characters. Especially, they are very useful when a big enthalpy difference between strong and weak binding site.

Here, *b* is the Langmuir-Freundlich parameter, and α is the Langmuir-Freundlich exponent (dimensionless) for two adsorption sites A and B. For calculation of mixture equilibrium, the mixed-gas Langmuir model is commonly used.[44]

$$N_i = \frac{N_{i,sat} b_i P_i}{1+\sum_{i=1}^{n} b_i P_i} \qquad \textit{(Eq. 8)}$$

The virial fitting is not suitable for adsorbent with coexisting strong and weak adsorption sites. The virial-type equation is proper to calculate zero-coverage adsorption heat. The zero coverage isosteric heat of adsorption gives the information for the strength of the strongest binding sites in the adsorbent. The virial-type equation is used to fit the gas sorption data, which is composed of parameters a_i and b_i that are independent of temperature.[45]

$$\ln P = \ln N + \frac{1}{T}\sum_{i=0}^{m} a_i N^i + \sum_{i=0}^{n} b_i N^i \qquad \textit{(Eq. 9)}$$

In (*Eq. 8*), P is pressure, N is the amount adsorbed gas, T is temperature, and *m* and *n* represent the number of coefficients required to adequately describe the isotherms . To estimate the values of the isosteric heat of gas adsorption, *(Eq. 9)* is applied, where R is the universal gas constant.

$$Q_{st} = -R\sum_{i=0}^{m} a_i N^i \qquad \textit{(Eq. 10)}$$

At a fixed temperature, gas isotherms can be fitted via least-squares regression to the virial model.

$$\ln(N/P) = A_0 + A_1 N + A_2 N^2 + A_3 N^3 + \cdots \qquad \textit{(Eq. 11)}$$

A_0, A_n etc. are virial coefficients. A_0 is related to the adsorbate-adsorbent interaction, whereas A_1 describes adsorbate-adsorbate interactions. Q_{st} for gas adsorption is calculated as a function of surface coverage by using van't Hoff isochore *(Eq. 12)*.

$$Q_{st} = R\ln\left(\frac{P_1}{P_2}\right)\frac{T_1T_2}{T_1 - T_2} \qquad \textit{(Eq. 12)}$$

1. 4. Calculation of Selectivity for Gases

Method 1. The selectivity factor is the molar ration of the adsorption quantities at the relevant partial pressures of the gases. The adsorption selectivity for CO_2 from the other gases is calculated from a selectivity factor using the single-component gas adsorption isotherm.[7]

$$S = \frac{N_1/N_2}{P_2/P_1} \qquad \textit{(Eq. 13)}$$

Where S is the selectivity factor, N_i represents the quantity adsorbed of component i, and P_i represents the partial pressures of component i.

Method 2. From a virial-type expression *(Eq. 8)*, the Henry constant (K_H) is calculated by *(Eq. 14)*. [45, 46]

$$K_H = \exp(-b_0)\cdot\exp(-a_0/T) \qquad \textit{(Eq. 14)}$$

The Henry's Law selectivity for gas component i over j at the same temperature is calculated based on *(Eq. 15)*.

$$S_{ij} = K_{Hi}/K_{Hj} \qquad \textit{(Eq. 15)}$$

Method 3. In the Langmuir equation, the Henry constant is obtained by *(Eq. 16)* and selectivity is calculated by *(Eq. 15)*. [47]

$$N = \frac{K_H P}{1 + \frac{K_H P}{N_{sat}}} \qquad \textit{(Eq. 16)}$$

$$\lim_{P \to 0} N = \lim_{P \to 0} \frac{K_H P}{1 + \frac{K_H P}{N_{sat}}} = K_H \qquad \textit{(Eq. 17)}$$

Based on the *(Eq. 17)*, the Henry constant is equivalent to the initial slope of the isotherm curve. The selectivity is also estimated by the ratio of initial slopes.

Method 4. Ideal adsorbed solution theory (IAST) has been used to predict the adsorption equilibria for components in a gaseous mixture using their respective pure-component isotherm parameters at the same temperature and on the same adsorbent.[48] The theory consists of a series of equations,

$$\pi_i^0(P_i^0) = \frac{RT}{A} \int_{p=0}^{P_i^0} \frac{n_i^0(p)}{P} dP \qquad \textit{(Eq. 18)}$$

$$P y_i = P_i^0 x_i \qquad \textit{(Eq. 19)}$$

$$x_i^0 = x_j^0 \qquad \textit{(Eq. 20)}$$

$$\sum x_i = 1 \qquad \textit{(Eq. 21)}$$

$$\sum y_i = 1 \qquad \textit{(Eq. 22)}$$

$$S_{ij} = P_i^0 \big/ P_j^0 \qquad \textit{(Eq. 23)}$$

In *(Eq. 18)*, n is the experimentally measured gas uptake as a function of pressure *P*, A is the available surface area, π^0 is the spreading pressures, and P_0 is the equilibrium pressure

of the single-component gas corresponding to π^0. The variable x_i and y_i are the adsorbed and gas phase mole fractions of gas *i*, respectively. *(Eq. 19)* is a definition of the spreading pressure for a single component gas adsorbate, while *(Eq. 20)* relateds the amount of adsorbed component *i* to the gas phase component for a given total pressure of the simulated multi-component gas stream. The spreading pressure is numerically calculated from the experimentally measured excess isotherms. *(Eq. 20)* is the statement of equilibrium, indicating that all pressures or temperatures must be equalized for equilibrium to be attained. The final equation yields the *i:j* gas selectivity *(Eq. 23)*. [49]

2. Experimental Section

General Methods. Anhydrous 1, 4-dioxane was purchased from Sigma Aldrich, and used without further purification. Other chemicals and solvents used in the syntheses were of reagent grade and were used without further purification. Infrared spectra were recorded with a Perkin Elmer 2000 FT-IR spectrophotometer. Elemental analyses were recorded with a Perkin Elmer 2400 Series II CHNS/O Analyzer. ^{1}H NMR spectra were measured on Bruker Advance DPX-300 spectrometer (300 MHz) at room temperature. Thermogravimetric analyses (TGA) and differential scanning calorimetry (DSC) were performed under N_2 (g) at a scan rate of 5 ^{o}C using a TGA Q50 and a DSC Q10 of TA instruments, respectively. Powder X-ray diffraction (PXRD) data were recorded on a Bruker D5005 diffractometer at 40 kV and 40 mA for Cu Kα (λ = 1.54050 Å) with a scan

speed of 0.5 ˚min^{-1} and a step size of 0.02 ˚ in 2θ.

Supercritical CO_2 Drying Method. Prior to drying, crystals as-synthesized, which were still in the mother liquor, were transferred to a vial (20 mL). The mother liquor was decanted and the crystals were washed briefly with pure solvent (2~15 mL). The crystals were placed inside the supercritical dryer together with the solvent, and the drying chamber was sealed. The temperature and pressure of the chamber were raised to 45 ^{o}C and 200 bar with CO_2, above the critical point (31.8 ^{o}C, 73 atm) of CO_2. The chamber was vented at a rate of 10 mL min^{-1} and then filled with CO_2 again. The cycles of refilling with CO_2, pressurizing, and venting were repeated for 6 h. After drying, the closed container with the dried crystals was transferred to a glove bag to prevent exposure of the crystals to air. The gas sorption isotherms of the samples were measured without further activation.

X-ray Crystallographic Analysis. Crystals of $[Zn_4O(NTN)_2]\cdot 10DMA\cdot 7H_2O$ (**SNU-150)** and $[Zn_5(NTN)_4\cdot(DEF)_2][(NH_2(C_2H_5)_2]_2\cdot 8DEF\cdot 6H_2O$ (**SNU-151)** were coated with Paratone-N oil and the diffraction data were measured at 100 K with synchrotron radiation (λ = 0.80003 Å for **SNU-150** and λ = 0.69999 Å for **SNU-151**) on an ADSC Quantum-210 detector at 2D SMC with a silicon (111) double crystal monochromator (DCM) at the Pohang Accelerator Laboratory, Korea. The *ADSC Q210 ADX program*[50] was used for data collection, **(SNU-150:** detector distance, 62 mm; omega scan, $\Delta\omega$ = 1 º; exposure time, 10 sec per frame) **(SNU-151:** detector distance, 70 mm; omega scan, $\Delta\omega$ = 1 º; exposure time, 10 sec per frame) and *HKL3000sm* (Ver. 703r)[51] was used for cell

refinement, reduction, and absorption corrections.

The diffraction data of $[Zn_4O(NTN)_2]$ (**SNU-150'),** which resulted by the treatment of $[Zn_4O(NTN)_2]\cdot 10DMA\cdot 7H_2O$ with supercritical CO_2, were collected at 100 K with an Enraf–Nonius Kappa CCD diffractometer (Mo K*a*, λ=0.71073, graphite monochromator). For the collection of X-ray diffraction data of **SNU-150'**, the crystal was coated with Paratone-N oil. Preliminary orientation matrices and unit cell parameters were obtained from the peaks of the first 10 frames and then refined by using the whole data set. Frames were integrated and corrected for Lorentz and polarization effects using *DENZO*.[51] The scaling and global refinement of crystal parameters were performed by using *SCALEPACK*.[51] No adsorption correction was made. The crystal structures of **SNU-150**, **SNU-151**, and **SNU-150'** were solved by direct methods[52] and refined by full-matrix least-square refinement using *SHELXL-97* program.[53] The hydrogen atoms were positioned geometrically by using a riding model. The electron densities of the disordered guest molecules were flattened by using the *SQUEEZE* option of *PLATON*.[54] In **SNU-150**, the overall framework was statistically disordered over two sites with 1:1 occupancies. Consequently, all the atoms were given by 0.5 occupancy except that Zn(1), O(1), O(1)', N(1), and N(1)', which sit on three-fold crystallographic axes, were given by the occupancy of 1/6. In **SNU-150',** the site occupancy factors were given as 0.33333 for Zn(1), O(1), N(1), and N(2) atoms, which sit on three-fold crystallographic axes.

Gas Sorption Measurements. The gas adsorption-desorption experiments were performed using an automated micropore gas analyzer, an Autosorb-3B (Quantachrome Instruments). All of the gases used were of 99.999% purity. **SNU-150'** and **SNU-151'**

were predesolvated by using supercritical CO_2 method at 45 ^oC for 8 h. The pre-dried solid was introduced to a gas sorption cell, whose weight was exactly measured, and then the gas sorption isotherms were measured. The sample weight was measured precisely after the measurement of gas sorption. Between the experiments with various gases, the out-gassing procedure was repeated for ca. 1 h. The N_2 gas sorption isotherms were monitored at 77 K by using liquid nitrogen, and the H_2 gas sorption isotherms were monitored at 77 K and 87 K, at each equilibrium pressure by the static volumetric method. The adsorption isotherms for CO_2 and CH_4 gases were measured at 195 K, 231 K, 273 K, and 298 K. The sorption properties, including pore volume, pore size, and surface area were analyzed by using Autosorb 1 for Windows 1.24 software.

Estimation Isosteric Heats of the H_2 Adsorption. The isosteric heats of the H_2 adsorption for **SNU-150'** and **SNU-151'** were estimated from the H_2 sorption data measured at 77 K and 87 K. A virial-type expression was used *(Eq 1)*, which is composed of parameters a_i and b_i that are independent of temperature. In eq. 1, P is the pressure in atm, N is the amount of adsorbed H_2 gas in mg g^{-1}, T is the temperature in K, a_i and b_i are the virial coefficients, and m and n represent the number of coefficients required to adequately describe the isotherms. An equation was fit using the R statistical software package.[55]

$$\ln P = \ln N + \frac{1}{T}\sum_{i=o}^{m} a_i N^i + \sum_{i=0}^{m} b_i N^i \qquad \textit{(Eq. 24)}$$

The values of the virial coefficients, a_0 through a_m, were then used to calculate the isosteric heat of adsorption using *(Eq. 25)*, where Q_{st} is the coverage-dependent isosteric heat of adsorption and R is the universal gas constant.

$$Q_{st} = -R\sum_{i=o}^{m} a_i N^i \qquad \textit{(Eq. 25)}$$

Estimation of Isosteric Heats of the CO_2 and CH_4 Adsorption. The CO_2 adsorption data of **SNU-150'** and **SNU-151'** at 195 K, 231 K, 273 K, and 298 K were fit to polynomial equation by using *Origin8* program, and the CH_4 adsorption data of **SNU-150'** and **SNU-151'** at 195 K, 231 K, 273 K, and 298 K were fit to Langmuir-Freundlich equation where N is amount of absorbed gas, N_{sat} is amount of adsorbed gas at saturation, P is pressure, and b and t are the constants. *(Eq. 26).* And then heat of adsorption was calculated by using Clausius-Clapeyron equation *(Eq. 27)* at each gas loading point.

$$\frac{N}{N_{sat}} = \frac{bP^{1/t}}{1+bP^{1/t}} \qquad \textit{(Eq. 26)}$$

$$\frac{\partial(\ln P)}{\partial(1/t)} = -\frac{Q_{st}}{R} \qquad \textit{(Eq. 27)}$$

Calculation of CO_2 separation parameters. CO_2 separation parameters were calculated by using ideal adsorbed solution theory (IAST),[48] which enables prediction of adsorption

equilibriums of the binary gas mixtures from the related single-component isotherms. According to IAST:

$$y_1 + y_2 = 1 \qquad \textit{(Eq. 28)}$$

$$x_1 + x_2 = 1 \qquad \textit{(Eq. 29)}$$

$$p_{mix} y_1 = p_1^o x_1 \qquad \textit{(Eq. 30)}$$

$$p_{mix} y_2 = p_2^o x_2 \qquad \textit{(Eq.31)}$$

$$\pi_1^o = \frac{RT}{A}\int_0^{p_1^o} n_1(p) d\ln p \qquad \textit{(Eq. 32)}$$

$$\pi_2^o = \frac{RT}{A}\int_0^{p_2^o} n_2(p) d\ln p \qquad \textit{(Eq. 33)}$$

$$\pi = \pi_1^o = \pi_2^o \qquad \textit{(Eq. 34)}$$

Where y_i is the mole fraction of component *i* in the bulk gas mixture, x_i is the mole fraction of component *i* in adsorbed gas mixture, p_{mix} is the total pressure of the bulk gas mixture, p_i^o is the bulk pressure of pure component *i* that corresponds to the spreading pressure π of the binary mixture, *R* is the universal gas constant, *T* is adsorption temperature, *A* is surface area of the adsorbent, $n_i(p)$ is amount adsorbed at pressure *p* for pure component *i*. From the *(Eq. 28-34)*, the following equation can be obtained:

$$\int_0^{\frac{p_{mix} y_1}{x_1}} n_1(p) d\ln p = \int_0^{\frac{p_{mix} y_2}{1-x_1}} n_2(p) d\ln p$$

(Eq 35)

Total adsorption amount of the gas mixture (n_Δ) is calculated by the following equation:

$$\frac{1}{n_\Delta} = \frac{1}{n_1(p_1^o)} + \frac{1}{n_2(p_2^o)} \qquad \textit{(Eq. 36)}$$

where $n_1(p_1^o)$ is the amount of component 1 adsorbed at spreading pressure π in the absence of component 2, and $n_2(p_2^o)$ is the amount of component 2 adsorbed at spreading pressure π in the absence of component 1.

The adsorption amount for component i (n_i^Δ) in the binary mixture adsorption is calculated by the following equation:

$$n_1^\Delta = n_\Delta x_1 \quad \textit{(Eq. 37)}$$

$$n_2^\Delta = n_\Delta x_2 \quad \textit{(Eq. 38)}$$

Adsorption selectivity of component 1 over component 2 (S_{12}) is calculated by the following equation:

$$S_{12} = \frac{x_1 y_2}{x_2 y_1} \quad \textit{(Eq. 39)}$$

To calculate the five CO_2 separation parameters mentioned in the text for flue gas separation by VSA method, gas mixture composition is assumed to be 1:9 CO_2/N_2, adsorption and desorption pressures are assumed to be 1 and 0.1 atm, respectively.

Assume that CO_2 is component 1, N_2 is component 2. For adsorption, p_{mix} is 1 atm, y_1 is 0.1, y_2 is 0.9, and the functions $n_i(p)$ can be obtained by fittings of the single-component adsorption isotherms with Allometric1 equation for **SNU-150'**, and polynomial equation for **SNU-151'** by using *Origin8* program. The x_1 can be then obtained by solving the *Eq. S12* with MATLAB software.[56] All other unknowns can be obtained from the x_1. The n_1^{Δ} obtained from *(Eq. 37)* is corresponding to the "**CO_2 uptake under adsorption condition**", the n_2^{Δ} obtained from *(Eq. 38)* is corresponding to the "N_2 uptake under adsorption condition", and S_{12} obtained from *(Eq. 39)* is corresponding to the "**selectivity under adsorption condition**". For desorption, p_{mix} is 0.1 atm, y_1 is 0.1, y_2 is 0.9, and the functions $n_i(p)$ can be obtained by fittings of the single-component adsorption isotherms with Allometric1 equation for **SNU-150'**, and polynomial equation for **SNU-151'** by using *Origin8* program. After solving the *(Eq. 35)*, all other unknowns can be obtained. The n_1^{Δ} obtained from *(Eq. 37)* is corresponding to the "CO_2 uptake under desorption condition", the n_2^{Δ} obtained from *(Eq. 38)* is corresponding to the "N_2 uptake under desorption condition", and S_{12} obtained from *(Eq. 39)* is corresponding to the "selectivity under desorption condition". The difference of n_1^{Δ} obtained under adsorption condition and under desorption condition is corresponding to the "**working CO_2 capacity**". The "**regenerability**" can be obtained by the following expression: $(n_1^{\Delta ads} - n_1^{\Delta des}) / n_1^{\Delta ads} \times 100$, where the superscripts ads and des mean calculation under adsorption and under desorption conditions, respectively. The difference of n_2^{Δ} obtained under adsorption condition and under desorption condition is corresponding to the

"working N_2 capacity". The "**sorbent selection parameter**" can be obtained from the following expression: $(S_{12}^{ads})^2 / S_{12}^{des}(n_1^{\Delta ads} - n_1^{\Delta des})/(n_2^{\Delta ads} - n_2^{\Delta des})$, where the superscripts ads and des mean calculation under adsorption and under desorption conditions, respectively. Thus, all the five parameters are obtained. The five CO_2 separation parameters for landfill gas separation by VSA method can be obtained in the same way, only except that the gas mixture composition changes to 1:1 CO_2/CH_4.

Synthesis of H_3NTN. H_3NTN (6,6',6"-nitrilotri-2-naphthoic acid) was prepared as follows by modifying the previously reported methods.[57]

Synthesis of methyl,6-(*N*,*N*-bis(6-methoxycarbonylnaphthyl)amino)-2-naphthoate. Under N_2 atmosphere, $Pd(OAc)_2$ (129 mg, 0.575 mmol) and rac-2,2'-bis(diphenylphosphino)-1,1'-binaphthyl) (rac-BINAP) (716 mg, 1.15 mmol) were dissolved in anhydrous 1,4-dioxane (100 mL). After stirring for 15 min, were added methyl 6-bromo-2-naphthoate (8.16 g, 30.8 mmol, 2.8 equiv.), methyl 6-amino-2-naphthoate (2.32 g, 11.5 mmol, 1 equiv.), and Cs_2CO_3 (5.63 g, 29.2 mmol, 2.5 equiv.). The solution was refluxed for five days, cooled to room temperature and diluted with CH_2Cl_2 (200 mL). Crude mixture was filtered through celite, concentrated by evaporation of the solvent, and then purified by silica gel column chromatography with n-hexane/CH_2Cl_2 (2:1, v/v) and then CH_2Cl_2 as eluents. The product was obtained as light yellow powder. ^{1}H NMR ($CDCl_3$): 3.99 (s, 9H), 7.44 (d, J = 8.8 Hz, 3H), 7.60-7.62 (m, 6H), 7.90 (d, J = 8.9 Hz, 3H), 8.03 (d, J = 8.6 Hz, 3H), 8.60 (s, 3H) ppm.

Synthesis of 6,6',6''-nitrilotri-2-naphthoic acid (H_3NTN acid). Methyl,6-(*N*,*N*-bis(6-methoxycarbonylnaphthyl)amino)-2-naphthoate was dissolved in MeOH and then saturated aqueous solution of NaOH was added till the pH of the solution became 8. The solution was heated at reflux for 1 day, and then the solvent was removed by evaporation. The crude product was dissolved with distilled water, and HCl was added till pH of the solution became 2. The solution was cooled to room temperature, and the solid formed was filtered off, washed with water, and dried in vacuo. Elemental analysis calcd. (%) for $C_{33}H_{21}NO_6$: C 75.13, H 4.01, N 2.66; found: C 73.01, H 4.06, N 2.56. ^{1}H NMR (DMSO-d_6): 7.40 (d J = 8.4 Hz, 3H), 7.64 (s, J = 35.7 Hz, 3H), 7.76 -7.90 (m, 6H), 8.00 (d, J = 9 Hz, 3H), 8.03 (d, J = 9 Hz, 3H), 8.46 (s, J = 25.8 Hz, 3H) ppm.

Synthesis of $[Zn_4O(NTN)_2]\cdot 10DMA\cdot 7H_2O$ (SNU-150). The DMA solution (DMA = dimethylacetamide, 1.5 mL) of $Zn(OAc)_2\cdot 2H_2O$ (67.3 mg, 0.3 mmol) and the DMA solution (1 mL) of H_3NTN (26.3 mg, 0.05 mmol) were added in a serum glass bottle. The bottle was sealed and heated in an oven at 90 ℃ for 24 h, which provided truncated octahedral shaped green crystals of $[Zn_4O(NTN)_2]\cdot 10DMA\cdot 7H_2O$. When DEF was used as solvent instead of DMA with the same reaction mixture, the product was formed as polycrystalline powder, whose PXRD data indicated that it had the same framework structure as **SNU-150**. Yield: 42.5 mg (73.2% based on H_3NTN). Elemental analysis calcd. (%) for $Zn_4C_{106}H_{140}N12O30$: C 54.78, H 6.07, N 7.23; found: C 54.46, H 5.90, N 7.33. FT-IR for 1 (KBr): ν$_{O-H}$, 3401; ν$_{O=C=O}$, 1626, 1587; ν$_{C-H(NTN)}$, 3053; ν$_{C-H(DMA)}$ 2931 cm-1.

Preparation of $[Zn_4O(NTN)_2]$ (SNU-150'). Prior to drying, crystals of as-synthesized **SNU-150** were transferred into a vial (20 mL) together with the mother liquor. The mother liquor was decanted and the crystals were washed briefly with pure DMA (2~15 mL). The sample was desolvated by using supercritical CO_2 fluid. Elemental analysis calcd. (%) for $Zn_4C_{66}H_{36}O_{13}N_2$: C 57.67, H 2.64, N 2.04; found: C 57.36, H 2.66, N 2.24. FT-IR for **SNU-150'** (KBr): νO=C=O, 1623, 1589; νC-$H_{(NTN)}$, 3052 cm^{-1}.

Synthesis of $[Zn_5(NTN)_4{\cdot}(DEF)_2][(NH_2(C_2H_5)_2]_2{\cdot}8DEF{\cdot}6H_2O$ (SNU-151). The DEF solution (1.5 mL) of $Zn(OAc)_2{\cdot}2H_2O$ (67.3 mg, 0.3 mmol) was mixed with the DEF solution (1 mL) of H_3NTN (26.3 mg, 0.05mmol) in a serum glass bottle, and then acetic acid (0.1 mL) was added. The reaction bottle was sealed and heated in an oven at 90 ℃ for 24 h, from which rhombus brown crystals of $[Zn_5(NTN)_4{\cdot}(DEF)_2][(NH_2(C_2H_5)_2]_2{\cdot}8DEF{\cdot}6H_2O$ were formed. Yield: 0.0306 mg (67.1% based on H_3NTN). Elemental analysis calcd. (%) for Zn5C190H208N16O35: C 61.80, H 5.95, N 6.07; found: C 61.39, H 5.77, N 5.95. FT-IR for **SNU-151** (KBr pellet): νO-H, 3429; νC-$H_{(NTN)}$, 3054; νO-C=O, 1625, 1594; νC-$H_{(NTN)}$, 2975, 2935; νN-$H_{(NH2(C2H5))+}$, 2875; νC=$O_{(DEF)}$, 1659 cm^{-1}. **SNU-150** and **SNU-151** are insoluble in common organic solvents.

Preparation of $[Zn_5(NTN)_4][(NH_2(C_2H_5)_2]_2$ (SNU-151'). Prior to activation, crystals of as-synthesized $[Zn_5(NTN)_4{\cdot}(DEF)_2][(NH_2(C_2H_5)_2]_2{\cdot}8DEF{\cdot}6H_2O$ were transferred to a vial (20 mL) together with the mother liquor. The mother liquor was decanted and the crystals

were washed briefly with pure DEF (2~15 mL). The sample was desolvated by using supercritical CO2 fluid. Elemental analysis calcd. (%) for $Zn_5C_{140}H_{96}O_{24}N_6$: C 65.34, H 3.27, N 3.76; found: C 65.81, H 3.39, N 3.80. FT-IR for **SNU-151'** (KBr pellet): ν$C\text{-}H_{(NTN)}$, 3050; ν$N\text{-}H(NH_2(C_2H_5))^+$, 2872; ν$O{=}C{=}O$, 1624, 1590; ν$C{=}O_{(NTN)}$, 1690 cm^{-1}.

3. Result and Discussion

Greenish truncated octahedral shaped crystals of **SNU-150** were prepared by heating a DMA solution of $Zn(OAc)_2 \cdot 2H_2O$ and H_3NTN at 90 ^oC for 24 h. Brown rhombus shaped crystals of **SNU-151** have been prepared by heating a DEF solution of $Zn(OAc)_2 \cdot 2H_2O$ and H_3NTN in the presence of acetic acid (DEF: acetic acid = 100:3 ~ 100:12, v/v) at 90 ^oC for 24 h. When the volume ratio of acetic acid/DEF was less than 2.4%, **SNU-150** was formed instead of **SNU-151** as evidenced by the powder X-ray diffraction (PXRD) patterns (Figure 10).

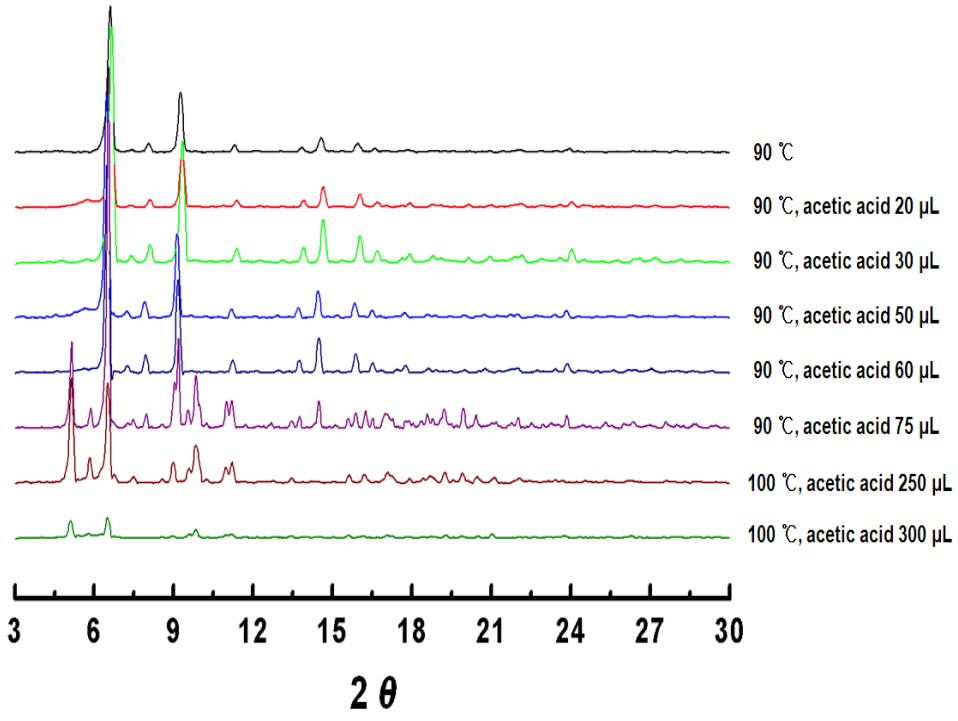

Figure 10. The PXRD patterns of products, which were formed from the solvothermal reaction of $Zn(OAc)_2\,2H_2O$ (67.3 mg, 0.3 mmol) and H_3NTN (26.3 mg, 0.05 mmol) in DEF in the presence of various amount of acetic acid.

The PXRD patterns indicate that **SNU-150** is formed when less than 75 uL (1.3 mmol) of acetic acid is added in the reaction mixture while **SNU-151** is formed when greater than 75 uL (1.3 mmol) but less than 300 uL (5.2 mmol) of acetic acid is added in the reaction mixture. Addition of a small amount of acetic acid in the reaction mixture gave rise to a totally different framework structure, since the acid hydrolyzed DEF solvent and produced diethyl ammonium cations, which induces the formation of the anionic framework. Interestingly, the acetate anions in the solution and the formate anions produced from the hydrolysis of DEF did not participate in the construction of the frameworks. TGA data of **SNU-150** reveals 43.8% weight loss at 20-400 ℃, corresponding to the loss of $2H_2O$ and 11DMA guest molecules per formula unit (calcd. 43.0%) (Figure 11). TGA data of **SNU-151** reveals 25.4% weight loss at 20-200 ℃ corresponding to the loss of $6H_2O$ and 8DEF guest molecules (calcd. 24.9%), followed by additional weight loss of 10.6% at 200-400 ℃, which corresponds to two coordinated DEF and two cationic $[NH_2(C_2H_5)_2]$ guests (calcd. 9.5%) (Figure 12).

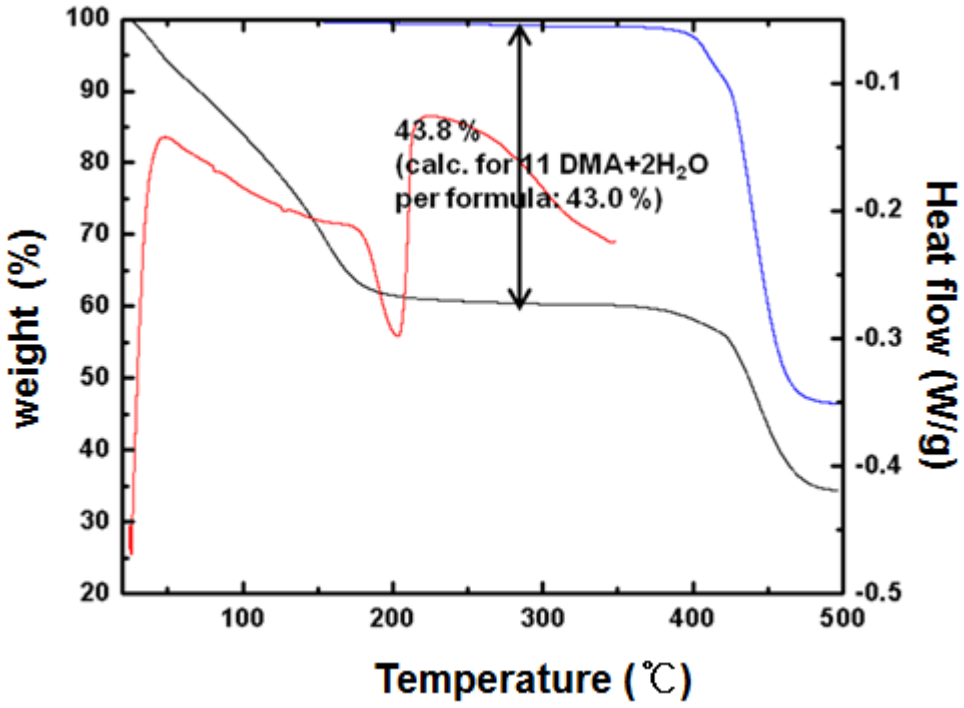

Figure 11. TGA traces of as-synthesized **SNU-150** (black) and guest-free **SNU-150'** (blue), together with DSC curve of **SNU-150** (red)**. SNU-150** reveals 43.8% weight loss at 20-400 ℃, corresponding to the loss of $2H_2O$ and 11DMA guest molecules per formula unit (calcd. 43.0%).

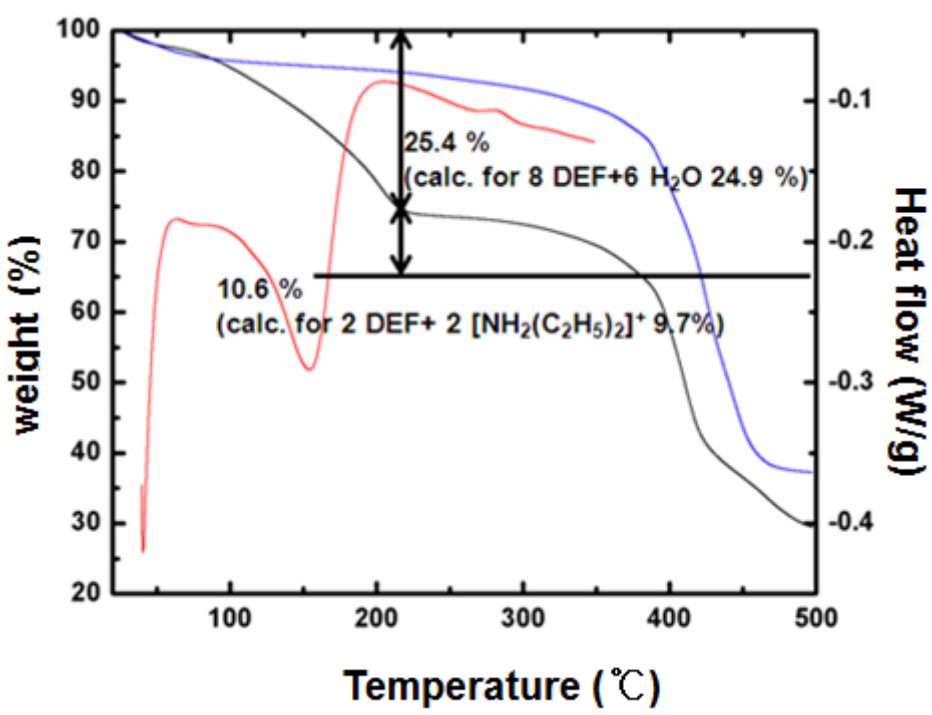

Figure 12. TGA and DSC (red) traces for as-synthesized **SNU-151** (black) and desolvated **SNU-151'** (blue). The weight loss of ca. 5% for **SNU-151'** corresponds to the moisture absorbed from air during the loading of the sample in the TG pan. **SNU-151** reveals 25.4% weight loss at 20-200 ℃ corresponding to the loss of $6H_2O$ and 8DEF guest molecules (calcd. 24.9%), followed by additional weight loss of 10.6% at 200-400 ℃, which corresponds to two coordinated DEF and two cationic $[NH_2(C_2H_5)_2]$ guests (calcd. 9.5%).

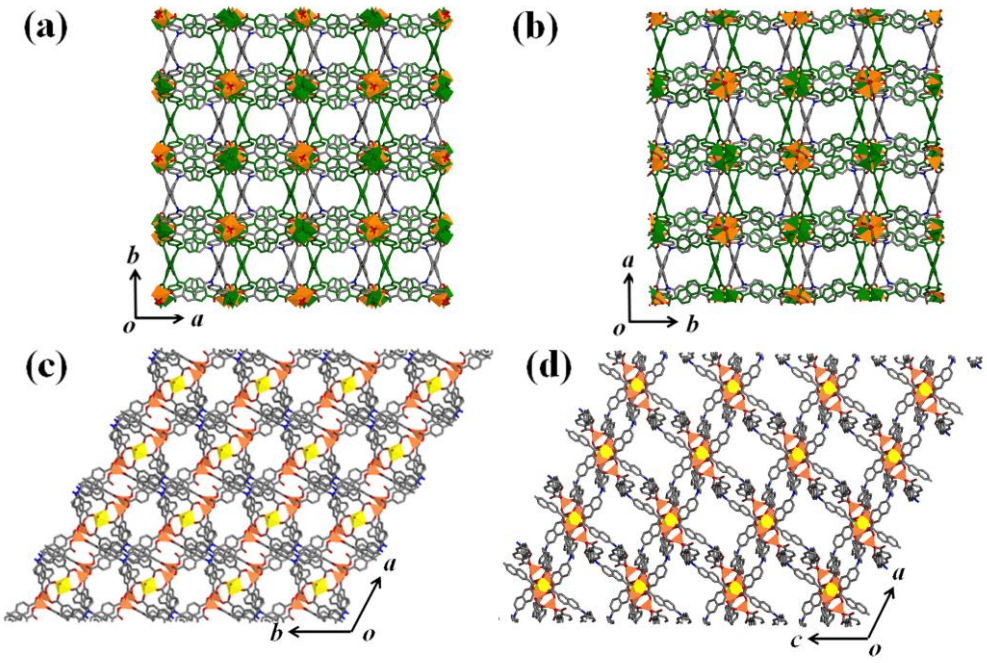

Figure 13. The X-ray crystal structures of **SNU-150**, **SNU-150'**, and **SNU-151**. (a) A view of **SNU-150** seen on the *ab* plane. (b) A view of **SNU-150'** seen on the *ab* plane. (c) A view of **SNU-151** seen on the *ab* plane. (d) A view of **SNU-151** seen on the *ac* plane. Tetrahedral Zn, orange; octahedral Zn, yellow.

In the X-ray structure of **SNU-150** (Figure. 14), $Zn_4O(CO_2)_6$ cluster acts as an octahedral secondary building unit (SBU) and NTN^{3-} acts as a triangular organic building block, which results in a (6.3)-connected net with a PdF_2 type net topology, similarly to the previous reports.[58-60] **SNU-150** is doubly interpenetrated and generates 3D channels that extend along the three orthogonal directions. The effective window size of the channels is 4.5 x 1.7 $Å^2$. The void volume of **SNU-150** is 49.5%, as calculated by PLATON.[61] When the single crystals of **SNU-150** were activated by using supercritical CO_2, desolvated

sample **SNU- 150'** was resulted, as evidenced by IR, EA, and TGA data (Figure.11).

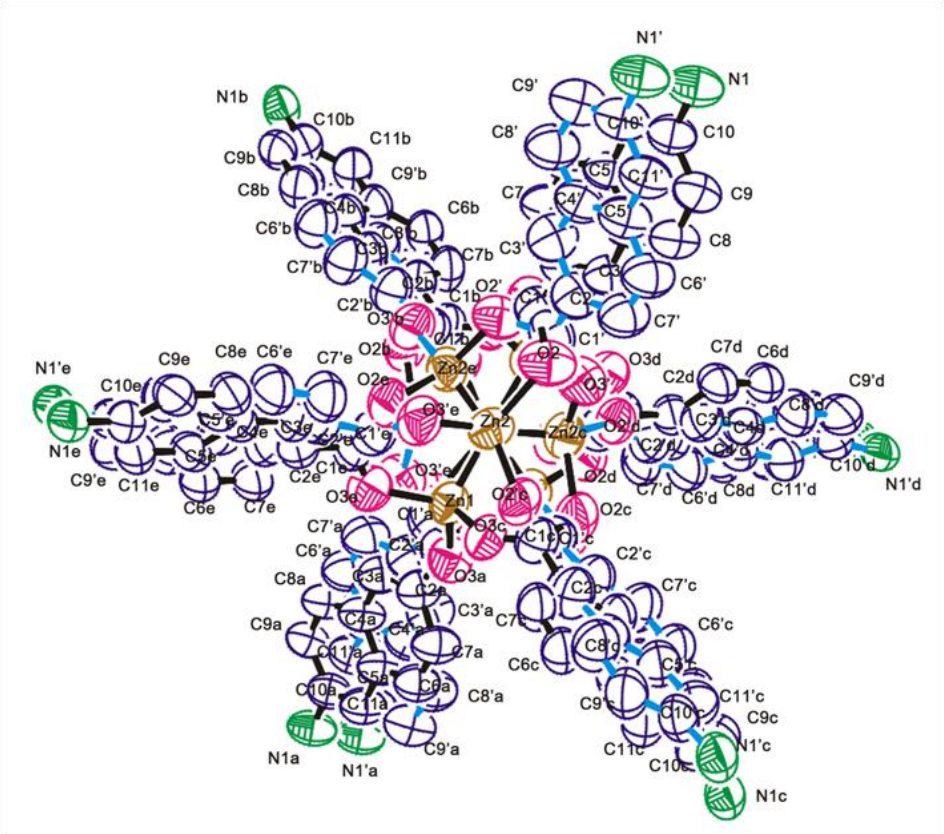

Figure 14. An ORTEP view of SNU-150 with atomic numbering scheme. Displacement ellipsoids are represented by 30% probability level. Symmetry operations: a, -x, -y+1, -z; b, -z, x+1/2, -y+1/2; c, z, -x+1/2, y-1/2; d, y-1/2, -z+1/2, -x; e, -y+1/2, z+1/2, x. The hydrogen atoms are deleted for clarity.

Interestingly, **SNU-150** underwent single-crystal-to-single-crystal transformation during the activation process (Figure. 11b). The activated **SNU-150'** exhibits a fine structure different from that of **SNU-150**. Many of the key dihedral angles become different from

those of **SNU-150** (Table 3), and thus the aperture size is enlarged compared to that of as-synthesized **SNU-150**, similarly to the case of **SNU-77S**.[58]

Table 2. Crystallographic data of **SNU-150, SNU-150'**, and **SNU-151** (Squeezed).

	SNU-150 [a]	**SNU-150'** [b]	**SNU-151** [c]
Formula	$Zn_4C_{66}H_{36}N_2O_{13}$	$Zn_4C_{66}H_{36}N_2O_{13}$	$Zn_5C_{142}H_{94}N_6O_{26}$
Crystal system	*Cubic*	*Cubic*	*Triclinic*
Space group	*Ia-3*	*Pa-3*	*P-1*
Formula weight	1326.45	1326.45	2627.08
a, Å	27.143(3)	27.3095(6)	16.158(3)
b, Å	27.143(3)	27.3095(6)	18.171(4)
c, Å	27.143(3)	27.3095(6)	18.955(4)
α, deg	90	90	99.19(3)
β, deg	90	90	106.28(3)
γ, deg	90	90	116.34(3)
V, Å^3	19997(4)	20367.7(8)	4518.8(27)
Z	8	8	1
ρ_{calcd}, g cm^{-3}	0.881	0.865	0.965
T, K	100(2)	120(2)	100(2)
λ, Å	0.80003	0.71073	0.69999
μ, mm^{-1}	1.316	0.970	0.646
Goodness-of-fit on F^2	1.271	0.999	1.539
F(000)	5360	5360	1346
Reflections collected	3912	11598	16832
Independent reflections	2081 [*R*(int) = 0.0141]	6011 [*R*(int) = 0.0463]	16832 [*R*(int) = 0.0000]
Completeness to	θ = 25.38, 96.1%	θ = 25.03, 100%	θ = 25.75, 93.0%
Data / restraints /	2081 / 759 / 255	6011 / 0 / 256	16832 / 3 / 808

parameters			
θ range for data collection, °	2.07 to 25.38	1.29 to 25.03	1.71 to 25.75
Diffraction limits (h, k, l)	-28<=h<=28, -20<=k<=20, -20<=l<=20	-32<=h<=32, -22<=k<=22, -22<=l<=22	0<=h<=20, -22<=k<=20, -23<=l<=22
Refinement method	Full-matrix least-squares on F^2	Full-matrix least-squares on F^2	Full-matrix least-squares on F^2
R_1, wR_2 [$I > 2\sigma(I)$]	0.1107,[a] 0.3329[b]	0.0771, [a] 0.2090[c]	0.1059, [a] 0.3253[b]
R_1, wR_2 (all data)	0.1328,[a] 0.3499[b]	0.0970, [a] 0.2187[c]	0.1120, [a] 0.3371[b]
Largest diff. peak and hole, e Å $^{-3}$	0.289, -0.350	4.170, -1.125	1.559, -3.119

[a] $R = \Sigma||F_o| - |F_c||/\Sigma|F_o|$. [b] $wR(F^2) = [\Sigma w(F_o^2 - F_c^2)2/ \Sigma w(F_o^2)^2]^{½}$ where $w = 1/[\ \sigma^2(F_o^2) + (0.2000P)^2 + (0.0000)P]$, $P = (F_o^2 + 2F_c^2)/3$ for **SNU-150**, and **SNU-151**, [c] $wR(F^2) = [\Sigma w(F_o^2 - F_c^2)2/\Sigma w(F_o^2)^2]^{½}$ where $w = 1/[\ \sigma^2(F_o^2) + (0.1469P)^2 + (0.0000)P]$, $P = (F_o^2 + 2F_c^2)/3$ for **SNU-150'.**

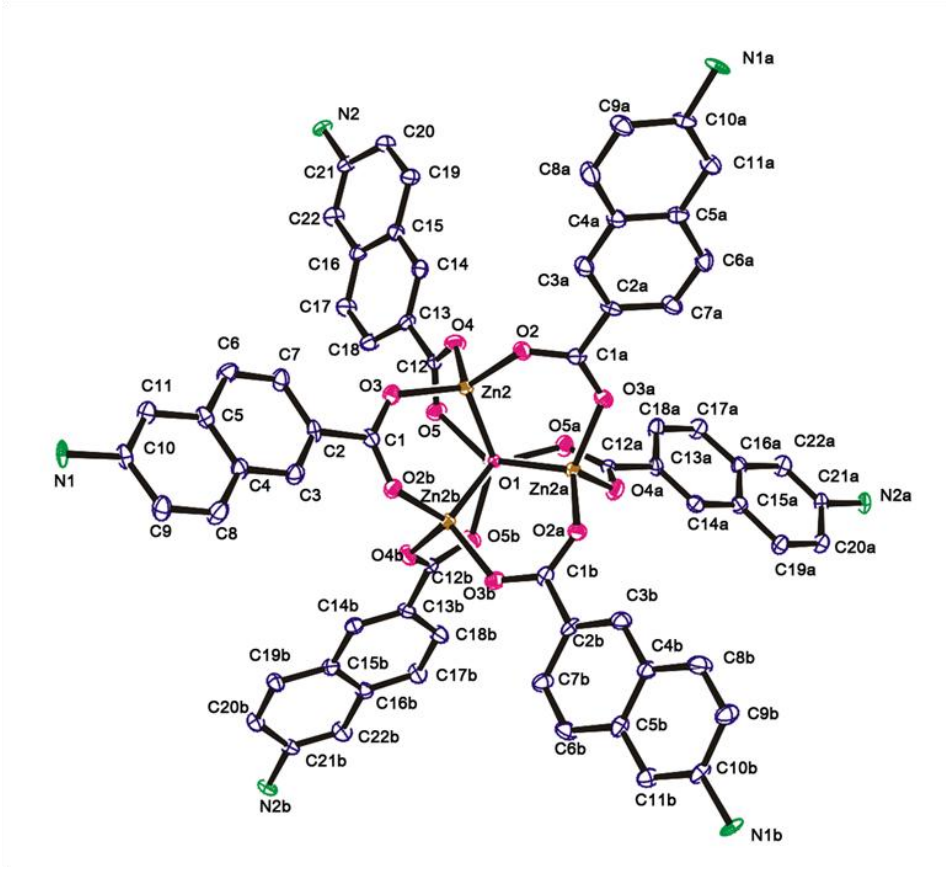

Figure 15. An ORTEP view of **SNU-150'** with atomic numbering scheme. Displacement ellipsoids are represented by 30 % probability level. Symmetry operations: a, z, x, y; b, y, z, x. The hydrogen atoms are deleted for clarity.

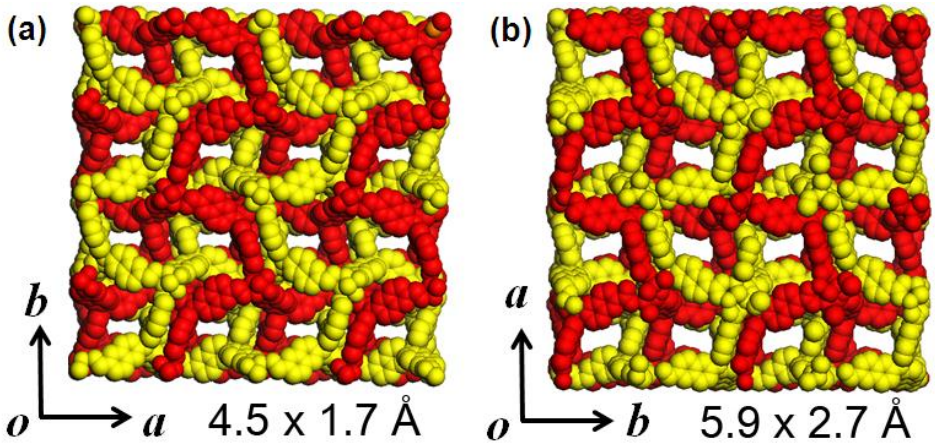

Figure 16. Comparison of the X-ray crystal structures of (a) **SNU-150** and (b) **SNU-150'**. Doubly interpenetrated networks are represented by two different colors, red and yellow. The numbers below each structure represent the effective aperture size.

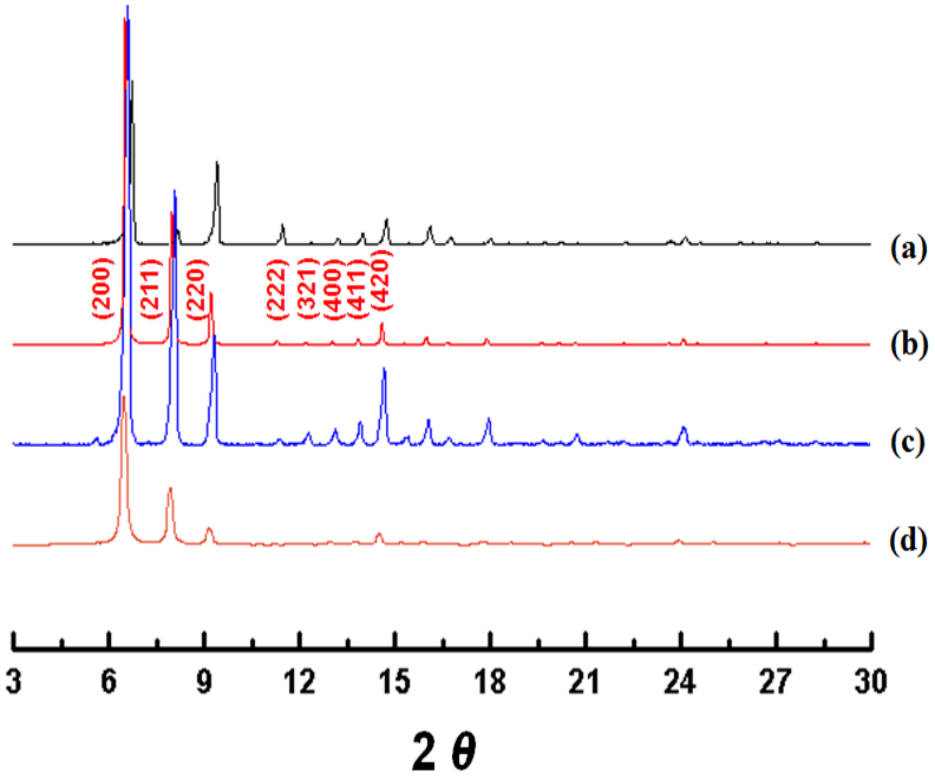

Figure 17. The PXRD patterns of (a) as-synthesized **SNU-150** (black), (b) simulated pattern based on single crystal X-ray data of **SNU-150** (red), (c) supercritical dried **SNU-150'** (blue), and (d) simulated supercritical dried **SNU-150'** (orange).

Table 3. Comparison of crystal structures for **SNU-150**, **SNU-150'**, and **SNU-151**.

MOF	Dihedral angle between naphthyl rings		π-π interaction	
	Naphthyl rings	Two Naphthyl	Shortest C–C	Dihedral Angle [˚]

	in a NTN^{3-}	rings trans to Zn_4O unit	Distance [Å]	
SNU-150	60.8(5.5)	0.00(37)	3.519(53)	1.96(36)
SNU-150'	54.8(1.3), 54.3(7)	11.2(1)	3.521(10)	1.10(13)
SNU-151	30.3(6), 46.7(8)	-	3.346(6)	29.2(1)

In the X-ray structure of **SNU-151**, there are crystallographically independent three Zn(II) centers (Zn1, Zn2, and Zn3), and they are linked in the sequence of Zn1-Zn2-Zn3-Zn2-Zn1 to form a Zn_5 cluster unit. Zn1 and Zn2 show a tetrahedral (td) coordination geometry by being coordinated with four carboxylate oxygen atoms of four different NTN^{3-} ligands (Figure 18a).

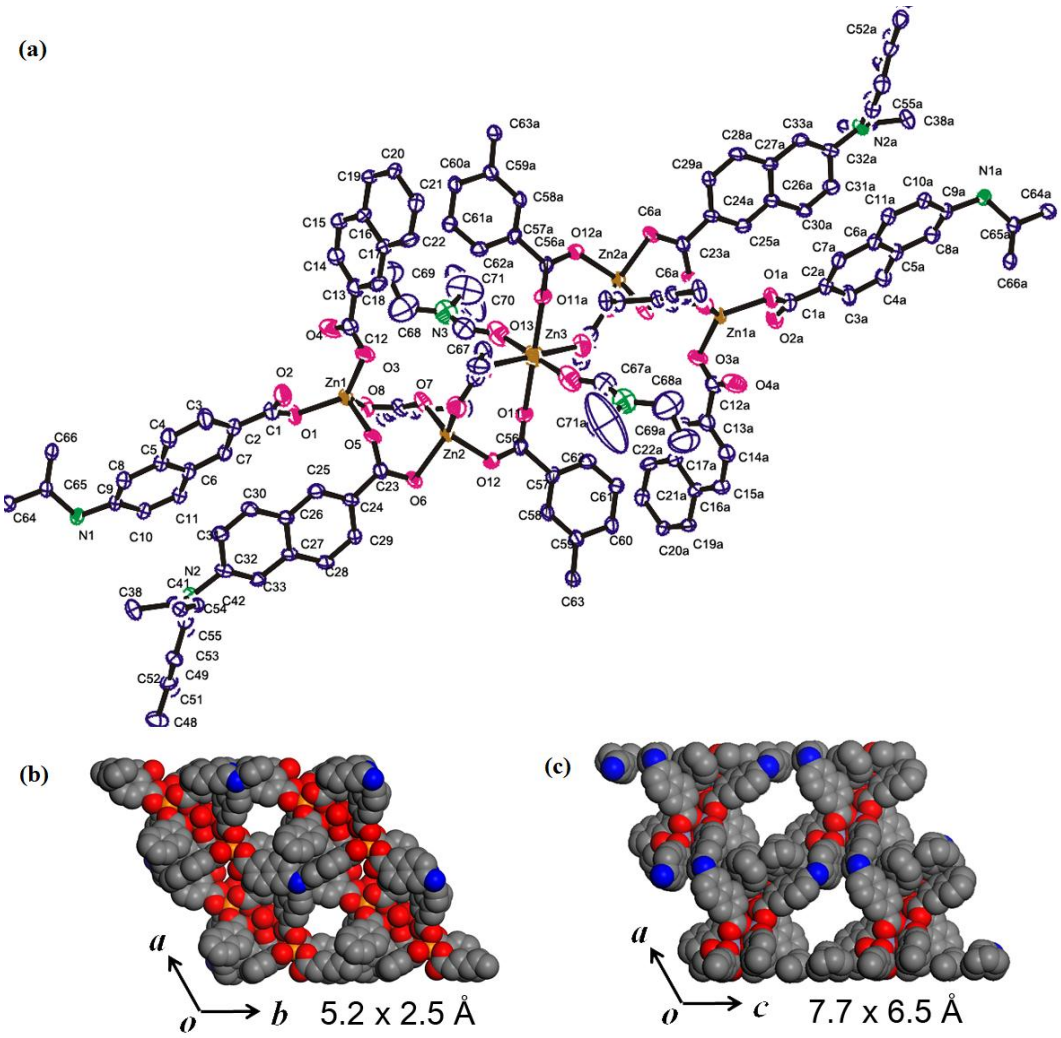

Figure 18. X-ray crystal structures of **SNU-151.** (a) An ORTEP view of **SNU-151** with atomic numbering scheme**.** Displacement ellipsoids are represented by 30% probability level. Symmetry operations: a, (-x+2, -y+2, -z+2). The hydrogen atoms are deleted for clarity. (b) A view seen on the *ab* plane, (c) A view seen on the *ac* plane.

Zn3 shows an octahedral coordination geometry by being coordinated with four carboxylate oxygen atoms of four different NTN^{3-} ligands and two oxygen atoms of DEF solvent molecules (Figure 18a). The Zn_5 cluster units are connected by carboxylate group to form a non-interpenetrated anionic 3D framework generating 2D channels. The effective window sizes of the square channels extending along the *ab* plane and of the cylindrical channels extending along the *ac* plane are 5.2 x 2.5 $Å^2$ and 7.7 x 6.5 $Å^2$, respectively (Fig. 15b, 15c). Since the Zn_5 metal cluster consists of five Zn(II) ions and twelve carboxylate groups, two counter cations should be included per formula unit. The chemical formula of **SNU-151** including two diethylammonium cations as guests was determined by the elemental analysis (EA) data as well as the IR spectrum showing ammonium peaks at 2875 cm^{-1}, since diethylammonium cations could not be refined by the single-crystal X-ray diffraction data due to the severe disorder. The void volume of **SNU-151** is 51.5% without considering the ammonium guests that could not be located by the X-ray diffraction study. When **SNU-151** was activated by using supercritical CO_2, two DEF molecules coordinated at Zn3 of **SNU-151** were removed together with the DEF and water guests solvent molecules included in the channels. The PXRD patterns indicate that the framework structure of **SNU-151'** changed significantly compared with that of as-synthesized **SNU-151** (Figure 19)

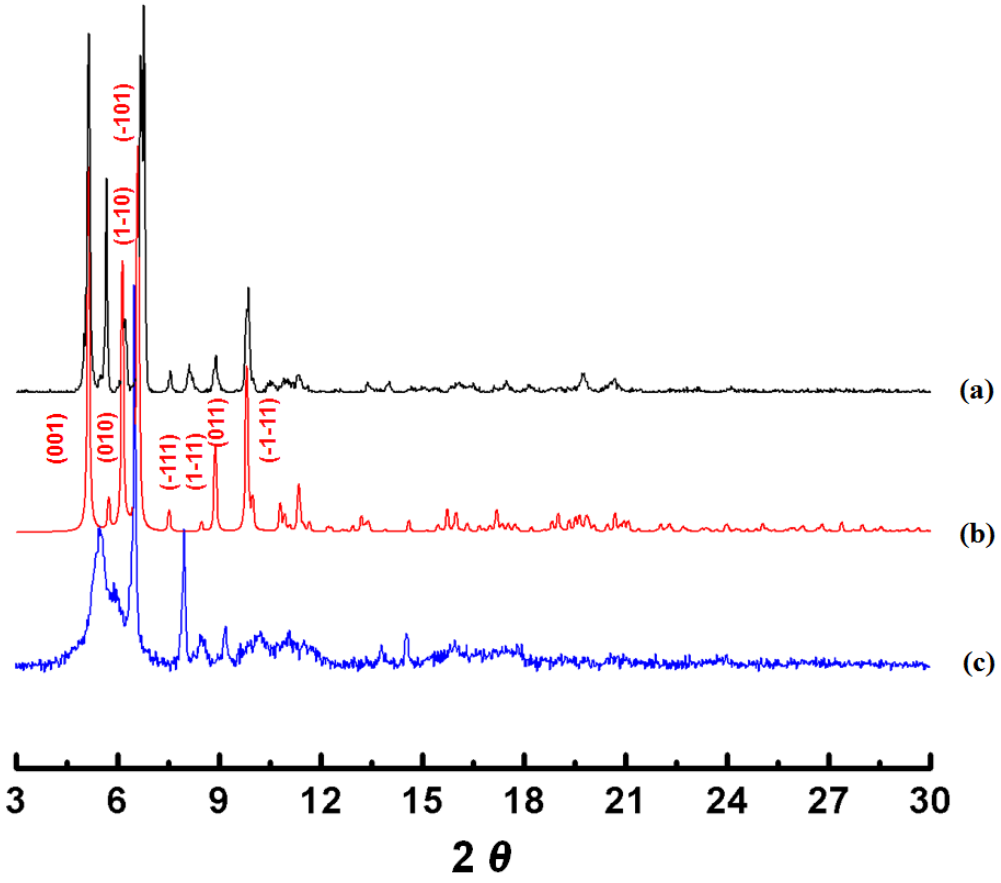

Figure 19. The PXRD patterns of (a) as-synthesized **SNU-151** (black), (b) simulated pattern from the single crystal data of **SNU-151** (red), (c) **SNU-151'** obtained by the treatment of **SNU-151** with supercritical CO_2 (blue).

The gas adsorption isotherms of **SNU-150'** and **SNU-151'** were measured for N_2, H_2, CO_2, and CH_4 gases, and the data are summarized in Table 4 together with the

comparison with the similar frameworks, **SNU-77S**[58] and **SNU-100'**[41] respectively.

Table 4. Comparisons of gas adsorption properties of **SNU-150'** and **SNU-151'** together with **SNU-77S** and **SNU-100'**.

Gas	T / K	P / atm	Adsorption capacity (wt%)			
			SNU-150'	**SNU-77S**	**SNU-151'**	**SNU-100'**
N_2	77	0.95	71.1	131	55.3	26.2
	298	1	0.546	0.40	0.519	0.624
H_2	77	1	1.54	1.79	2.00	1.81
	87	1	1.00	1.01	1.24	1.30
Q_{st} of H_2 adsorption	($kJmol^{-1}$)		5.04-4.65	7.05	6.27-5.82	8.14-7.08
CO_2	195	1	78.6	169	67.8	45.2
	231	1	40.5	130	56.0	37.2
	273	1	12.0	8.21	22.2	19.9
	298	1	6.09	3.94	14.1	14.1
Q_{st} of CO_2 adsorption ($kJmol^{-1}$)			17.1-16.5	19.9-19.4	27.1-21.0	29.3-27.7
CH_4	195	1	11.1	8.70	11.3	10.4
	231	1	3.15	4.12	7.30	7.57
	273	1	1.29	1.20	2.00	2.56
	298	1	0.859	0.62	1.24	1.41
Q_{st} of CH_4 adsorption ($kJmol^{-1}$)			12.8-12.3	14.3-14.2	18.2-16.6	26.5-22.4
Ref.			This work	58	This work	41

The N_2 sorption isotherms of **SNU-150'** and **SNU-151'** show type I curves, characteristic

for the microporous materials. **SNU-150'** shows a small hysteresis of type H-4 in the desorption curve, which may be associated with the narrow slit-like pores (Fig. 16a).[38] The BET (Langmuir) surface areas of **SNU-150'** and **SNU-151'** are 1852 (1945) m^2g^{-1} and 1563 (1674) m^2g^{-1}, respectively. The pore volumes estimated by applying the Dubinin- Radushkevich (DR) equation are 0.717 cm^3g^{-1} for **SNU-150'** and 0.614 cm^3g^{-1} for **SNU-151'**. The pore-size distributions based on Horvath-Kawazoe (HK) method suggest that **SNU-150'** and **SNU-151'** have the pore sizes of 6.18 Å and 6.08 Å, respectively (Figure 21).[39,62,63]

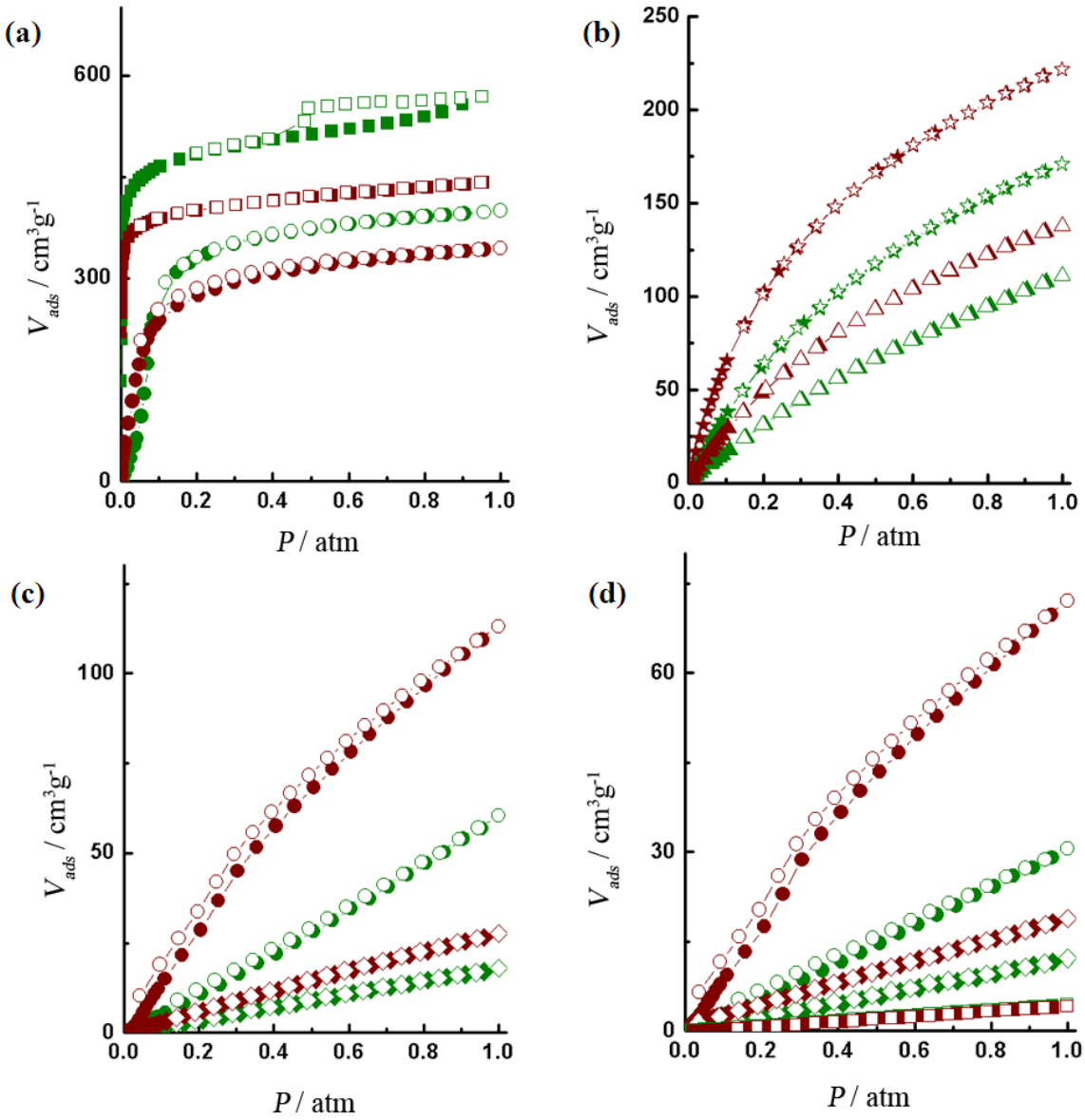

Figure 20. Gas sorption isotherms for **SNU-150'** (green) and **SNU-151'** (wine). (a) N_2 at 77 K (square) and CO_2 at 195 K (circle). (b) H_2 at 77 K (star) and 87 K (triangle). (c) CO_2 (circle) and CH_4 (diamond) at 273 K. (d) CO_2 (circle), CH_4 (diamond), and N_2 (square) at 298 K. Filled shape, adsorption; open shape, desorption.

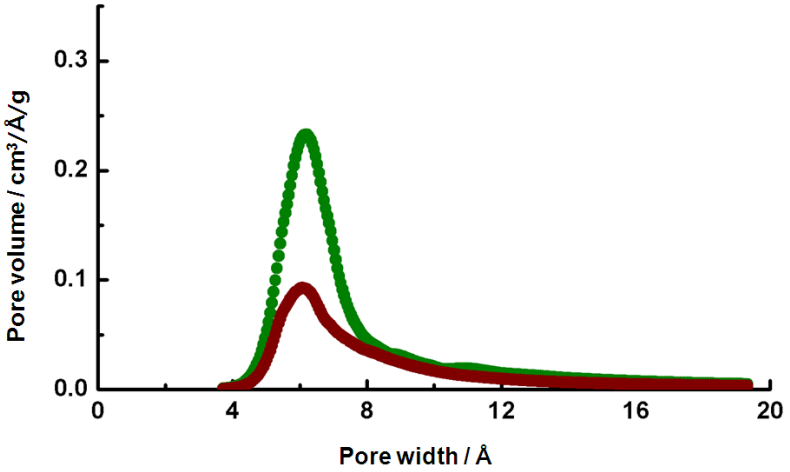

Figure 21. Pore size distributions of **SNU-150'** (green), and **SNU-151'** (brown)**,** estimated from the N_2 sorption data at 77 K by Horvath-Kawazoe (HK) method .

The H_2 adsorption capacities of **SNU-150'** and **SNU-151'** are 1.54 wt% and 2.00 wt%, respectively, at 77 K and 1 atm (Figure 20b). The isosteric heats (Q_{st}) of the H_2 adsorption estimated from the isotherms measured at 77 K and 87 K by using a virial equation[45] are 5.04 ~ 4.65 $kJmol^{-1}$ for **SNU-150'** and 6.27 ~ 5.82 $kJmol^{-1}$ for **SNU-151'**, depending on the degree of H_2 loading (Figure. 22b, 23b). depending on the H_2 loading.

As shown in Table 4, the CO_2 and CH_4 gas adsorption capacities of **SNU-151'** at 1 atm and T > 231 K are also higher than those of **SNU-150'**. At 298 K and 1 atm, **SNU-151'** adsorbs 14.1 wt% of CO_2, which is ca. 2.3 times higher than the CO_2 uptake capacity (6.09 wt%) of **SNU-150'** (Figure. 24).

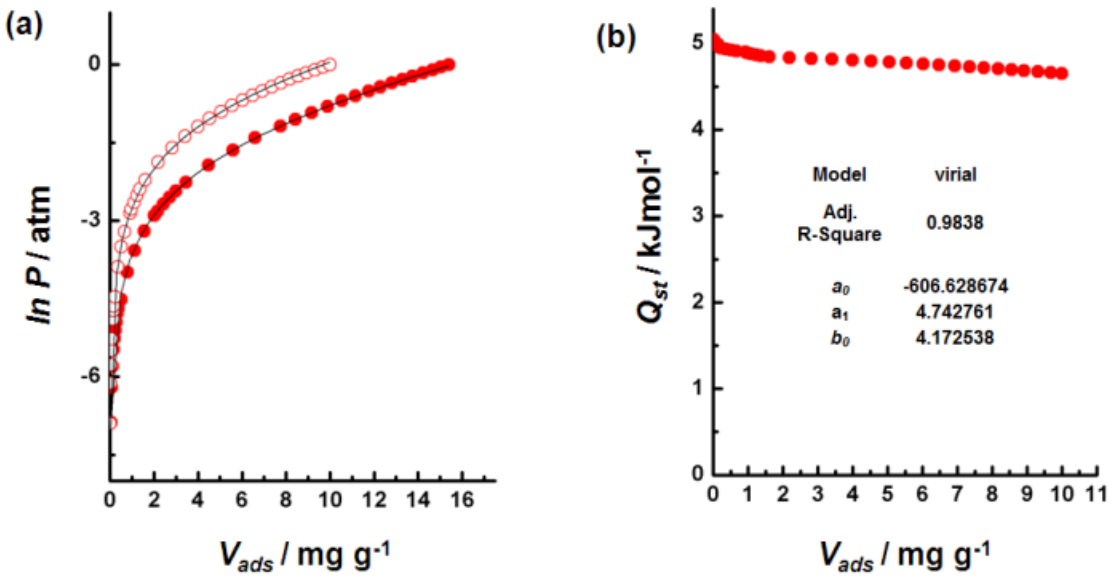

Figure 22. (a) The virial equation fits for H_2 adsorption isotherms of **SNU-150'** measured at 77 K (filled shapes) and 87 K (open shapes). (b) Isosteric heats of the H_2 adsorption in **SNU-150'** depending on the H_2 loading.

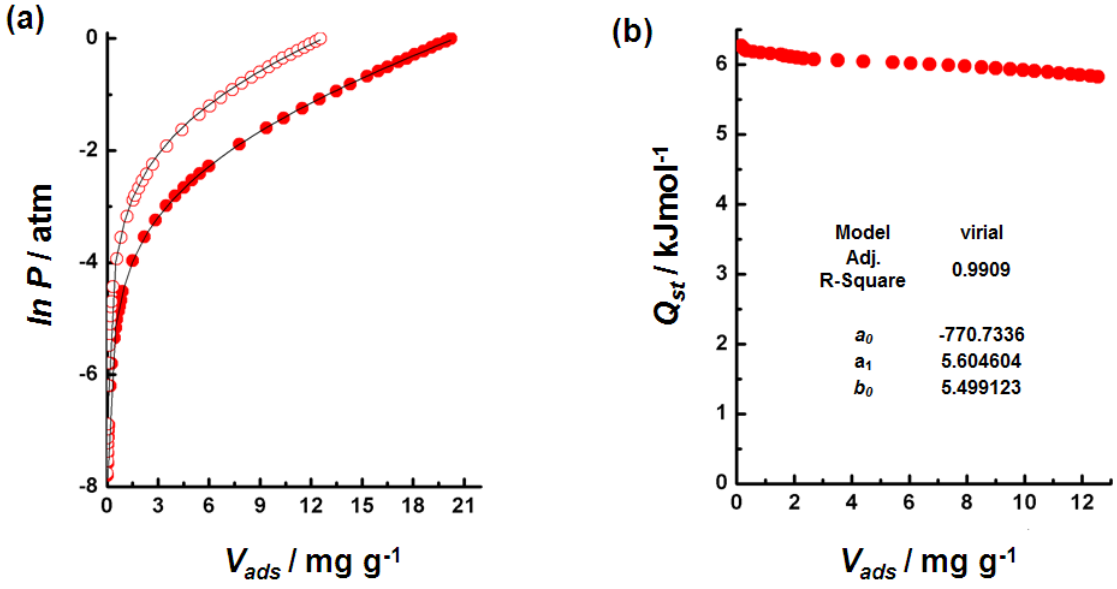

Figure 23. (a) The virial equation fits for H_2 adsorption isotherms of **SNU-151'** measured at 77 K (filled shapes) and 87 K (open shapes). (b) Isosteric heats of the H_2 adsorption in **SNU-151'**

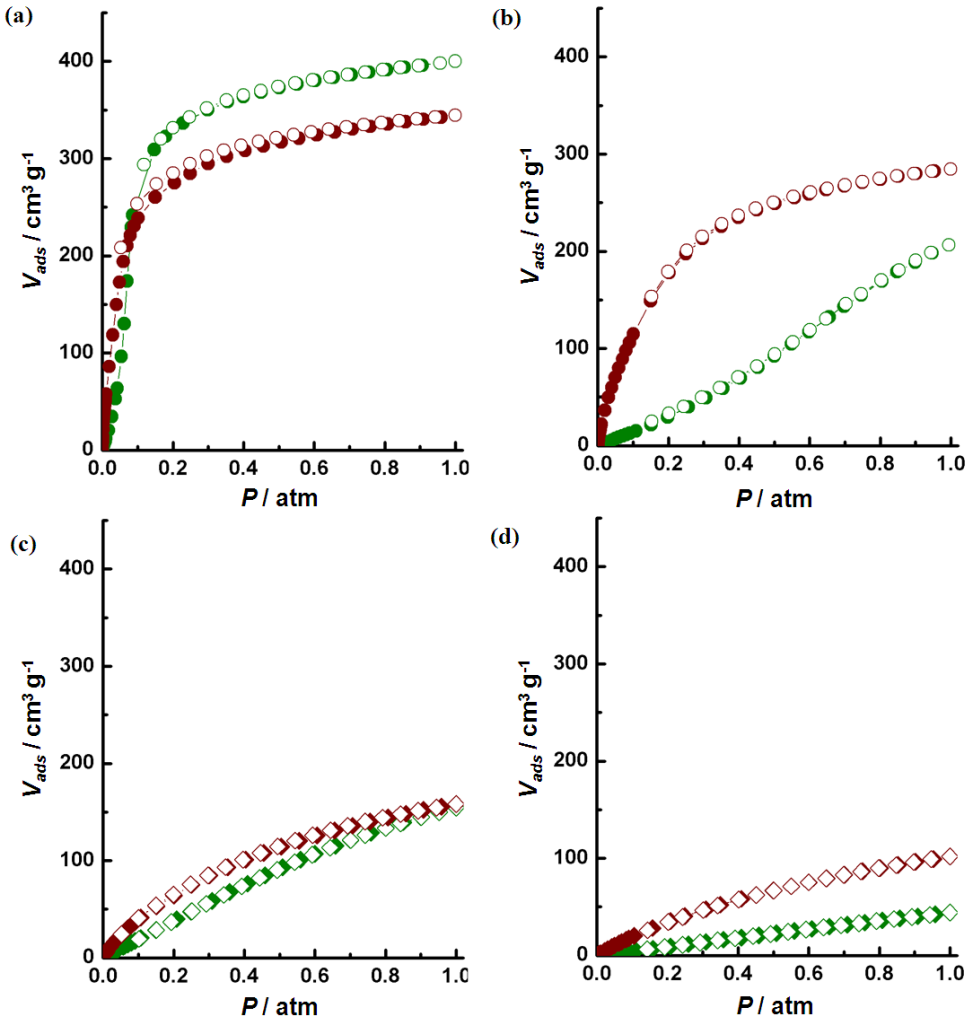

Figure 24. CO_2 and CH_4 gas sorption isotherms of **SNU-150'** (green) and **SNU-151'** (wine). (a) CO_2 at 195 K (circle), (b) CO_2 at 231 K (circle), (c) CH_4 at 195 K (diamond), and (d) CH_4 at 231 K (diamond). Filled shape, adsorption; open shape, desorption.

The Q_{st} values of CO_2 and CH_4 adsorptions were calculated by using the Clausius–

Clapeyron equation, applying the polynomial equation and Langmuir-Freundlich equation, respectively, to the adsorption isotherms measured at 195, 231, 273, and 298 K. The Q_{st} values of the CO_2 and CH_4 adsorptions in **SNU-151'** are 27.1~21.0 kJ mol^{-1} and 18.2~16.6 kJ mol^{-1}, respectively, which are also higher than those (17.1~16.5 and 12.8~12.3 kJ mol^{-1}, respectively) in **SNU-150'**.

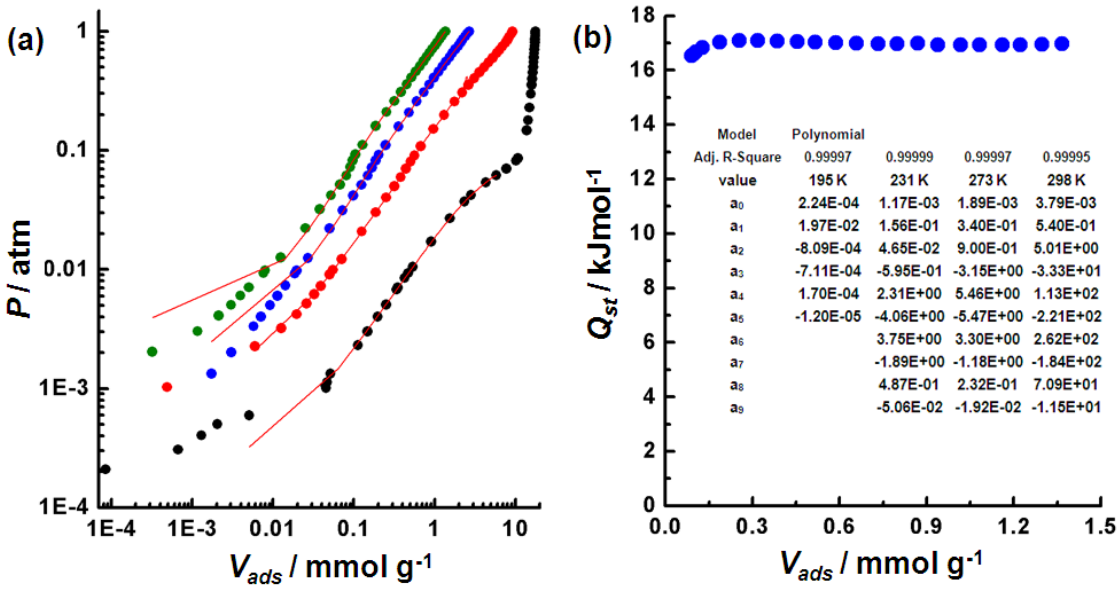

Figure 25. (a) CO_2 adsorption isotherms of **SNU-150'** measured at 195 K (black), 231 K (red), 273 K (blue), and 298 K (green), and their fits to polynomial equation on a logarithmic scale. (b) Isosteric heats of the CO_2 adsorption in **SNU-150'** depending on the CO_2 loading.

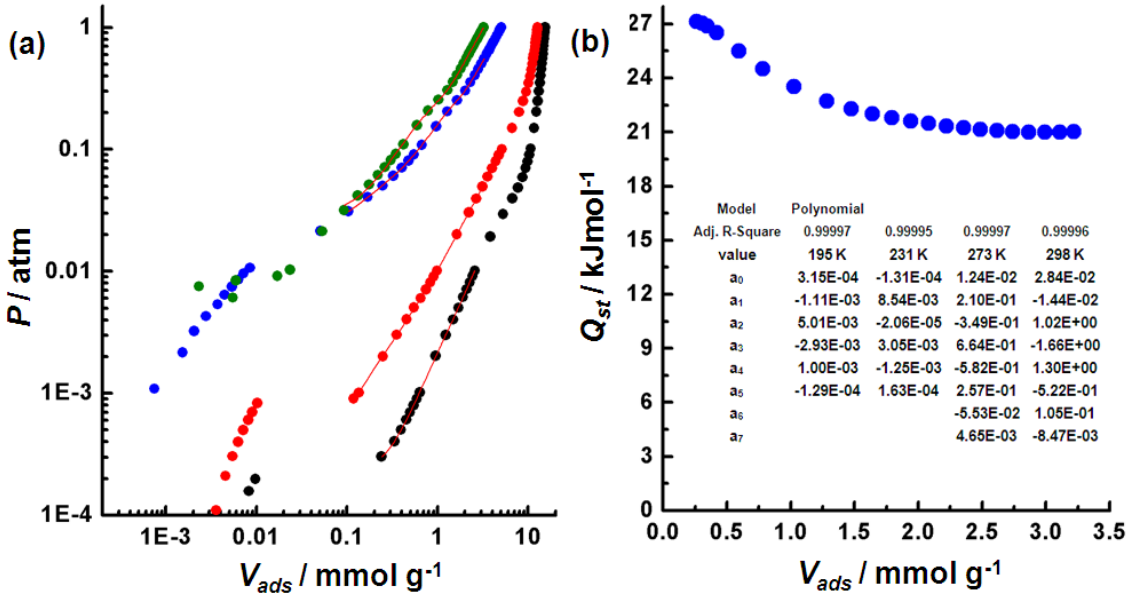

Figure 26. (a) CO_2 adsorption isotherms of **SNU-151'** measured at 195 K (black), 231 K (red), 273 K (blue), and 298 K (green), and their fits to polynomial equation on a logarithmic scale. (b) Isosteric heats of the CO_2 adsorption in **SNU-151'** depending on the CO_2 loading.

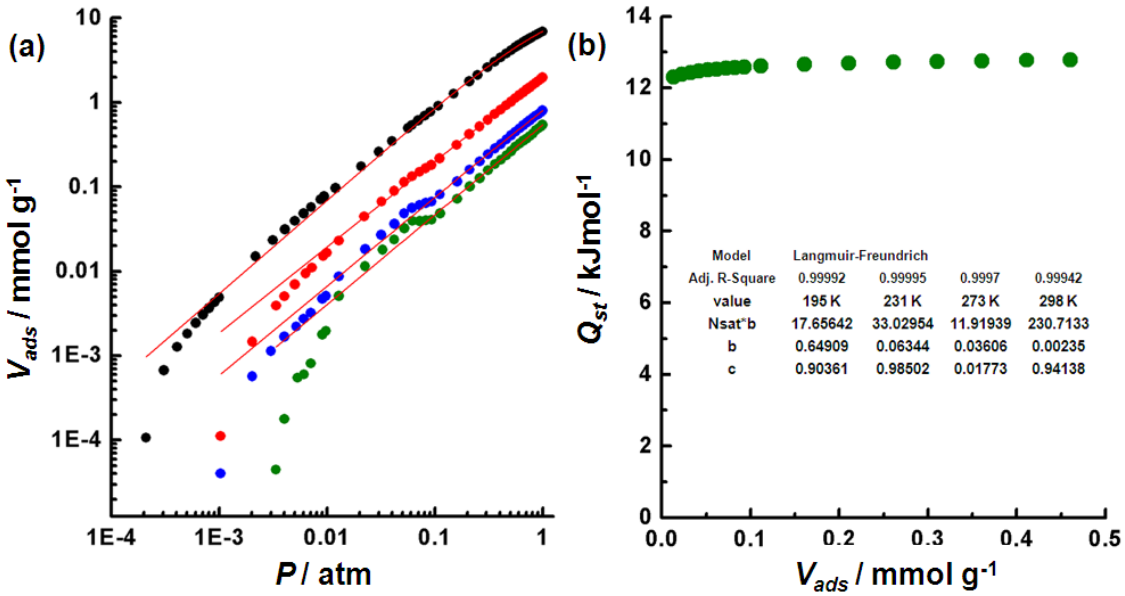

Figure 27. (a) CH_4 adsorption isotherms of **SNU-150'** measured at 195 K (black), 231 K (red), 273 K (blue), and 298 K (green), and their fits to Langmuir-Freundlich equation on a logarithmic scale. (b) Isosteric heat of the CH_4 adsorption in **SNU-150'** depending on the CH_4 loading.

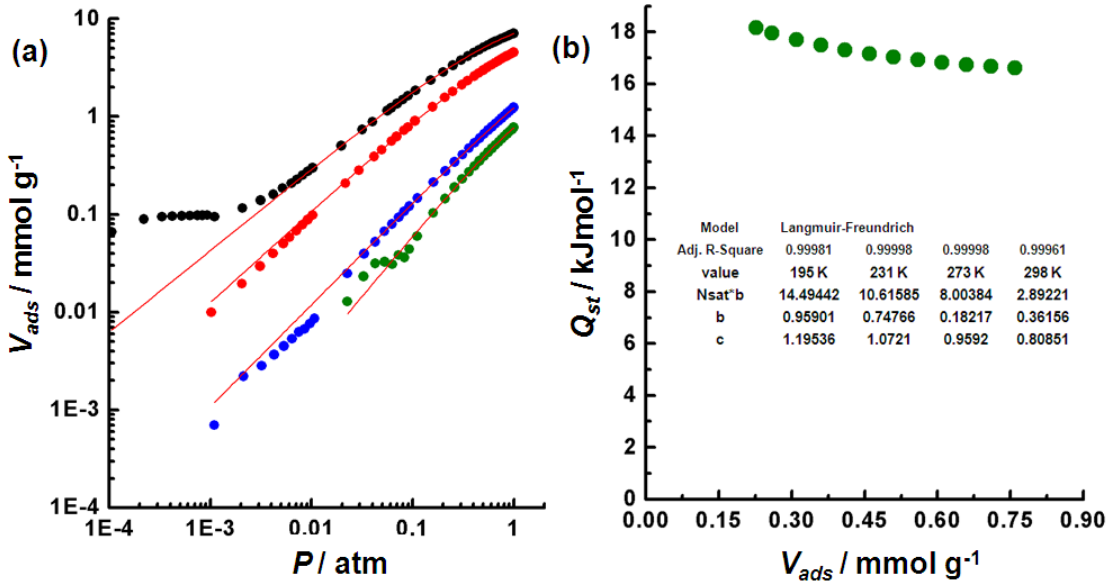

Figure 28. (a) CH_4 adsorption isotherms of **SNU-151'** measured at 195 K (black), 231 K (red), 273 K (blue), and 298 K (green), and their fits to Langmuir-Freundlich equation on a logarithmic scale. (b) Isosteric heat of the CH_4 adsorption in **SNU-151'** depending on the CH_4 loading.

Higher uptake capacities and higher Q_{st} values for the H_2, CO_2, and CH_4 adsorptions in **SNU-151'** than in **SNU-150'** must be attributed to the stronger interaction of those gas molecules with the anionic framework and diethylammonium cationic guests included in **SNU-151'**, compared to the interaction with the neutral framework **SNU-150'**, in addition to that the pore size (6.18 Å) of **SNU-151'** is a little bit smaller than that (6.08 Å) of **SNU-150'**. It has been reported that the charged frameworks show improved gas sorption properties compared to neutral ones.[41] When the gas adsorption properties of **SNU-150'** are compared with those of **SNU-77S**,[58] which also has PdF_2 topology, **SNU-150'** adsorbs much less amount of N_2 and H_2 gases at 77 K and 1 atm as well as less amount of CO_2 gas at 195 K and 1 atm than **SNU-77S**. This must be attributed to smaller surface area (1852 m^2g^{-1}) of **SNU-150'** than that (3670 m^2g^{-1}) of **SNU-77S**. When the gas adsorption properties of **SNU-151'** are compared with those of **SNU-100'**, which has anionic framework with diethylammonium cations, **SNU-151'** is much better than **SNU-100'**.[41] This can be explained by the higher surface area (1563 m^2g^{-1}) of **SNU-151'** than that (814 m^2g^{-1}) of **SNU-100'**. However, at 298 K and 1 atm, CO_2 and CH_4 gas uptake capacities of **SNU-150'** and **SNU-151'** became comparable to those of **SNU-77S** and **SNU-100'**, respectively. **SNU-150'** and **SNU-151'** adsorb CO_2 gas selectively at 298 K while they hardly adsorb N_2 gas (Fig. 20d, S2). The CO_2/N_2 adsorption selectivity values are 5.4 - 6.4 depending on the pressure (up to 1 atm) for **SNU-150'** and 30.0 for **SNU-151'**, as

calculated by using the ideal adsorbed solution theory (IAST) by assuming that flue gas has CO_2:N_2 volume ratio of 9:1 (Figure. 29b, 30b).

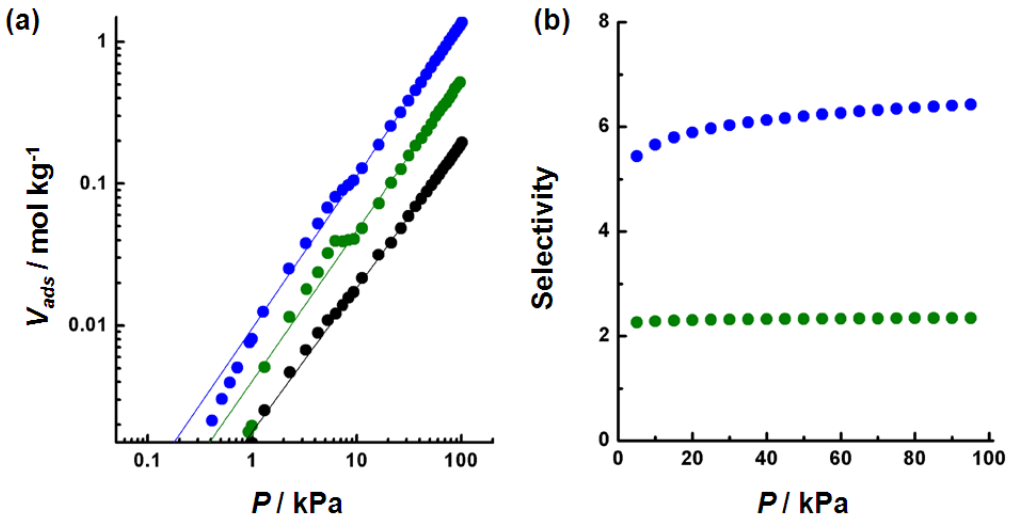

Figure 29. (a) CO_2 (blue), CH_4 (olive), and N_2 (black) adsorption isotherms of **SNU-150'** measured at 298 K, and their fits to Allometric1 equation on a logarithmic scale. (b) IAST selectivity of the CO_2 / N_2 (blue), and CO_2 / CH_4 (olive) adsorption in **SNU-150'** depending on the pressure.

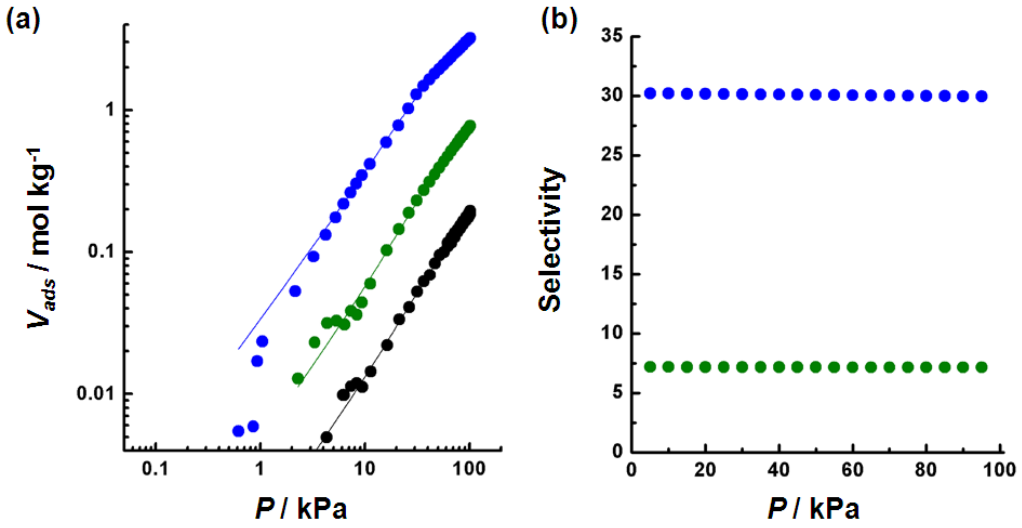

Figure 30. (a) CO_2 (blue), CH_4 (olive), and N_2 (black) adsorption isotherms of **SNU-151'** measured at 298 K, and their fits to Allometric1 equation on a logarithmic scale. (b) IAST selectivity of the CO_2 / N_2 (blue), and CO_2 / CH_4 (olive) adsorption in **SNU-151'** depending on the pressure.

The present result is consistent with our previous report that anionic framework (**SNU-100'**) with cationic guests showed very high CO_2/N_2 uptake selectivity.[41] The CO_2/N_2 adsorption selectivity of **SNU-151'** is higher than those of **SNU-100'** (26.5)[41] and $H_3[(Cu_4Cl)_3(BTTri)_8]$ (21.0).[64]

4. Conclusion

We have prepared two different porous MOFs, **SNU-150** and **SNU-151**, from the same metal and organic building blocks but in the presence and absence of acetic acid. **SNU-150** is a neutral framework whereas **SNU-151** is an anionic framework including diethylammonium guests. **SNU-150** undergoes a single-crystal-to-single-crystal transformation upon guest removal, which affords **SNU-150'** having slightly altered structure. Upon guest removal from **SNU-151**, which affords **SNU-151'**, **SNU-151'** shows higher uptake capacities for H_2, CO_2, and CH_4 gases than **SNU-150',** despite its smaller surface area (BET, 1563 $m^2 g^{-1}$) than that (BET, 1852 $m^2 g^{-1}$) of **SNU-150'** as well as higher isosteric heats of those gas adsorptions. Furthermore, **SNU-151'** shows significantly higher CO_2/N_2 adsorption selectivity at 298 K than **SNU-150'**. The results suggest that we should prepare the charged frameworks instead of neutral ones for gas storage and gas separation applications.

5. Supporting Information

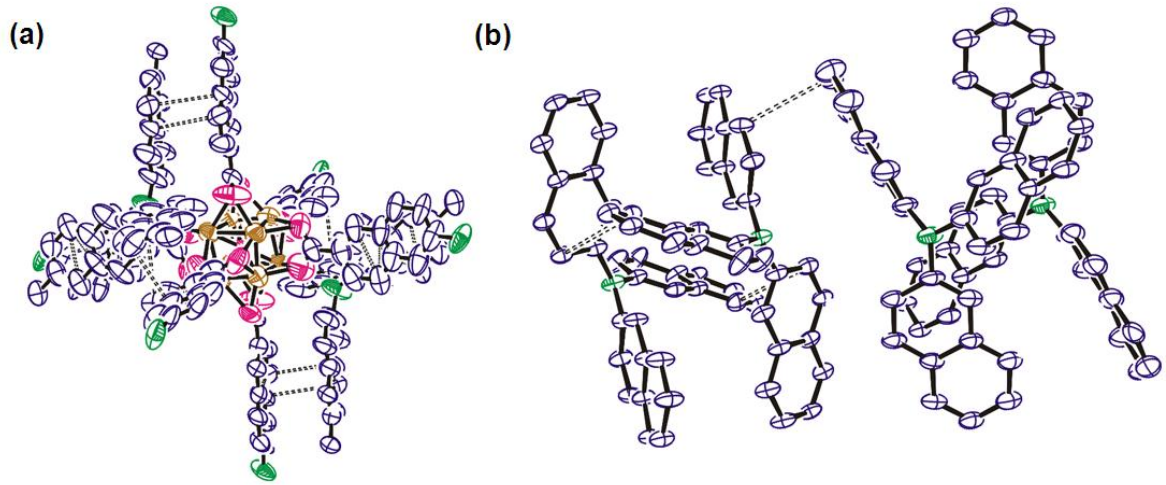

Figure S1. π-π interactions in **SNU-150** and **SNU-151**. (a) Face-to-face π-π interactions in **SNU-150**. (b) Edge-to-face π-π interactions in **SNU-151.**

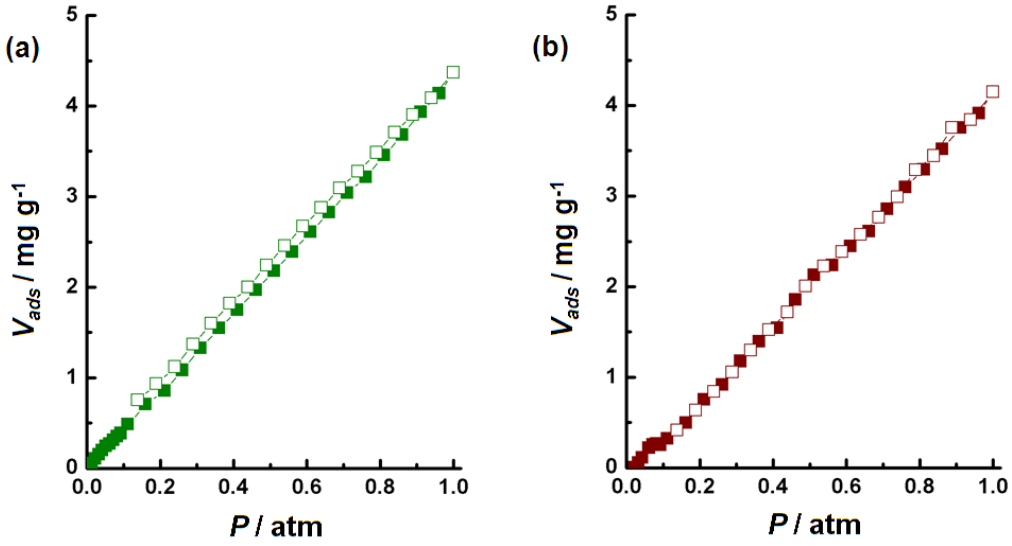

Figure S2. N_2 sorption isotherms of **SNU-150'** (green) and **SNU-151'** (wine) at 298 K. (a) **SNU-150'**, (b) **SNU-151'**. Filled shape, adsorption; open shape, desorption.

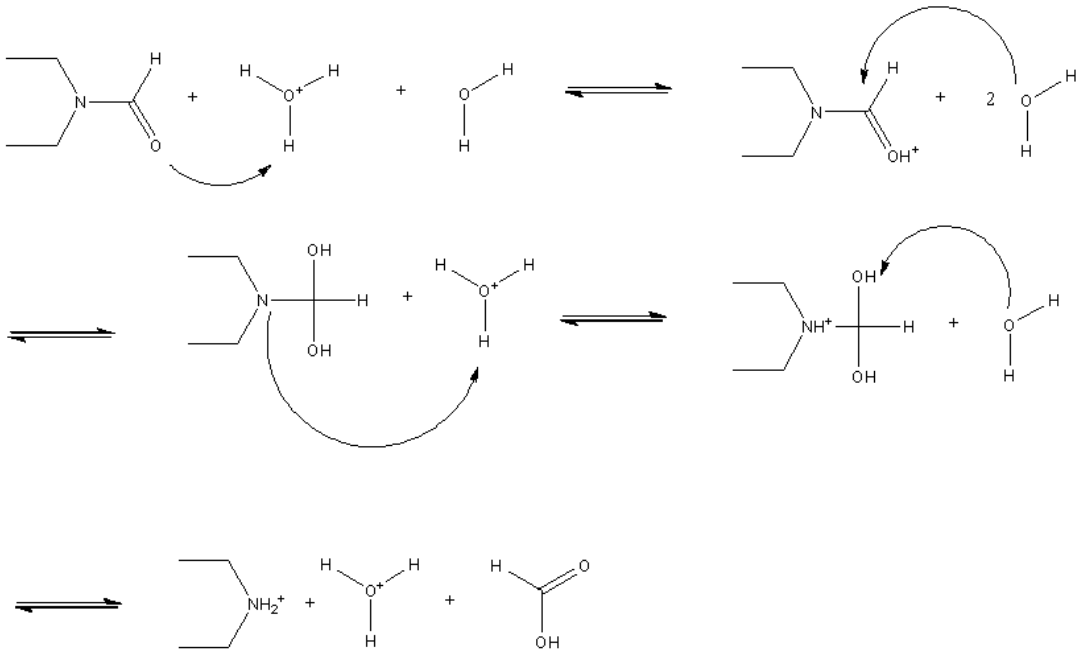

Figure S3. Protonation and Hydrolysis of DMF in Acidic Conditions.

The acidcatalyzed DMF hydrolysis can be described as a four step reaction according to the mechanism.[65]

.

Table S1. IAST parameters of **SNU-151'**.

Model	Polynomial		
Adj. R-Square	0.99982	Value	Standard Error
CO_2 298 K ads	Intercept	0	--
	b1	0.03326	0.00128
	b2	4.53E-04	6.95E-05
	b3	-9.49E-06	1.18E-06
	b4	4.83E-08	6.19E-09
Adj. R-Square	0.99986	Value	Standard Error
CH_4 298 K ads	Intercept	0	--
	b1	0.00462	2.77E-04
	b2	1.30E-04	1.51E-05
	b3	-1.79E-06	2.56E-07
	b4	7.92E-09	1.34E-09
Adj. R-Square	0.99908	Value	Standard Error
N_2 298 K ads	Intercept	0	--
	b1	0.0011	1.88E-04
	b2	2.55E-05	9.86E-06
	b3	-3.08E-07	1.62E-07
	b4	1.29E-09	8.26E-10

6. Reference

1. R. K. Pachauri, and A. Reisinger, IPCC Fourth Assessment Report (Intergovernmental Panel on Climate Change), 2007.

2. M. P. Suh, H. J. Park, T. K. Prasad, and D. W. Lim, *Chem Rev*, 2012, **112**, 782-835.

3. J. Sculley, D. Yuan, and H.-C. Zhou, *Energy Environ. Sci.*, 2011, **4**, 2721-2735.

4. R. B. Getman, Y.-S. Bae, C. E. Wilmer, and R. Q. Snurr, *Chem. Rev.*, 2012, 703-723.

5. H. J. Park, Y. E. Cheon, and M. P. Suh, *Chem-Eur J*, 2010, **16**, 11662-11669.

6. Y. Liu, Z. U. Wang, and H. -C. Zhou, *Greenhouse Gases: Science and Technology*, 2012, **2**, 239-259.

7. K. Sumida, D. L. Rogow, J. A. Mason, T. M. McDonald, E. D. Bloch, Z. R. Herm, T.-H. Bae, and J. R. Long, *Chem. Rev.*, 2012, **112**, 724-781.

8. J.-R. Li, Y. Ma, M. C. McCarthy, J. Sculley, J. Yu, H.-K. Jeong, P. B. Balbuena, and H.-C. Zhou, *Coord. Chem. Rev.*, 2011, **255**, 1791-1823.

9. T. K. Kim, and M. P. Suh, *Chem. Commun*, 2011, **47**, 4258-4260.

10. T. K. Prasad, D. H. Hong, and M. P. Suh, *Chem.-Eur J*, 2010, **16**, 14043-14050.

11. M. Kim, J. F. Cahill, J. Fei, K. A.Prather, and S. M. Cohen, *J. Am. Chem. Soc.*, 2012, **134**, 18082-18088.

12. P. Horcajada, T. Chalati, C. Serre, B. Gillet, C. Sebrie, T. Baati, J. F. Eubank, D. Heurtaux, P. Clayette, C. Kreuz, J. -S. Chang, Y. K. Hwang, V. Marsaud, P. -N. Bories, L. Cynober, S. Gil, G. Férey, P. Couvreur, and R. Gref, *Nature Materials*, 2010, **2**, 172-178.

13. R. C. Huxford, J. D. Rocca, and W. Lin, *Current opinion in chemical biology*, 2010, **14**, 262-268.

14. J. Lee, O. K. Farha, J. Roberts, K. A. Scheidt, S. T. Nguyen, and J. T. Hupp, *Chem. Soc. Rev.*, 2009, **38**, 1450-1459.

15. Inventory of U.S. Greenhouse Gas Emissions and Sinks: 1990–2006, Environmental Protection Agency, Washington DC, 2008.

16. O. K. Farha, I. Eryazici, N. C. Jeong, B. G. Hauser, C. E. Wilmer, A. A. Sarjeant, R. Q.

Snurr, S. T. Nguyen, A. O. Yazaydin, and J. T. Hupp. *J. Am. Chem. Soc.*, 2012, **134**, 15016-15021.

17. O. K. Farha, and J. T. Hupp, *Acc. Chem. Res.*, 2010, **43**, 1166-1175.

18. Q. Gao, Y. -B. Xie, J. -R. Li, D. -Q. Yuan, A. A. Yakovenko, J. -H. Sun, and H. -C. Zhou, *Crystal Growth & Design*, 2012, **12**, 281-288.

19. H. Li, M. Eddaoudi, M. O'Keeffe, and O. M. Yaghi, *nature*, 1999, **402**, 276-279.

20. M. Eddaoudi, H. Li, and O. M. Yaghi, *J. Am. Chem. Soc.*, 2000, **122**, 1391-1397.

21. S. S. Kaye, A. Dailly, O. M. Yaghi, and J. R. Long, *J. Am. Chem. Soc.*, 2007, **129**, 14176-14177.

22. J. L. C. Rowsell, and O. M. Yaghi, *J. Am. Chem. Soc.*, 2006, **128**, 1304-1315.

23. M. Eddaoudi, J. Kim, N. Rosi, D. Vodak, J. Wachter, M. O'Keeffe, and O. M. Yaghi, *Science*, 2002, **295**, 469-472.

24. H. Deng, C. J. Doonan, H. Furukawa, R. B. Ferreira, J. Towne, C. B. Knobler, B. Wang, and O. M. Yaghi, *Science*, 2010, **327**, 846-850.

25. Z. Wang, and S. M. Cohen, *Chem. Soc Rev.*, 2009, **38**, 1315-1329.

26. K. K. Tanabe, and S. M. Cohen, *Chem. Soc. Rev.*, 2011, **40**, 498-519.

27. Z. Wang, and S. M. Cohen, *J. Am. Chem. Soc.*, 2007, **129**, 12368-12369.

28. Z. Wang, and S. M. Cohen, *J. Am. Chem. Soc.* , 2009, **131**, 16675-16677.

29. M. Savonnet, D. Bazer-Bachi, N. Bats, J. Perez-Pellitero, E. Jeanneau, V. Lecocq, C. Pinel, and D. Farrusseng, *J. Am. Chem. Soc.*, 2010, **132**, 4518-4519.

30. S. J. Garibay, and S. M. Cohen, *Chem. Commun*, 2010, **46**, 7700-7702.

31. S. Bernt, V. Guillerm, C. Serre, and N. Stock, *Chem. Commun.*, 2011, **47**, 2838-2840.

32. A. Vimont, J. -M. Goupil, J. -C. Lavalley, M. Daturi, S. Surble´, C. Serre, F. Millange, G. Fe´rey, and N. Audebrand, *J. Am. Chem. Soc.*, 2006, **128**, 3218-3227.

33. M. Dinca, and J. R. Long, *Angew. Chem., Int. Ed*., 2008, **47**, 6766 – 6779.

34. W. Zhou, H. Wu, and T. Yildirim, *J. Am. Chem. Soc.*, 2008, **130**, 15268–15269.

35. P. D. C. Dietzel, V. Besikiotis, and R. Blom, *Journal of Materials Chemistry*, 2009, **19**, 7362-7370.

36. B. Chen, S. Xiang, and G. Qian, *Acc. Chem. Res.*, 2010, **43**, 1115-1124.

37. S. S. -Y. Chui, S. M.-F. Lo, J. P. H. Charmant, A. G. Orpen, and I. D. Williams, *Science*, 1999, **283**, 1148-1150.

38. F. Rouquerol, J. Rouquerol and K. Sing, *Adsorption by Powdors and Porous Solids Principles, Methodology and Applications*, Academic Press, San Diego, CA, 1999.

39. G. Horvath, and K. Kawazoe, *J. Chem. Eng. Japan.*, 1983, **16,** 470-475.

40. Y. G. Lee, H. R. Moon, Y. E. Cheon, and M. P. Suh, *Angew. Chem., Int. Ed.*, 2008, **47**, 7741-7745.

41. H. J. Park, and M. P. Suh, *Chem. Sci*, 2013, **4**, 685-690.

42. A. P. Nelson, O. K. Farha, K. L. Mulfort, and J. T. Hupp, *J. Am. Chem. Soc.*, 2009, **131**, 458-460.

43. M. Eddaoudi, H. Li, and O. M. Yaghi, *Adsorption*, 2000, **6**, 275-286.

44. D. M. Ruthven, S. Farooq, K. S. Knaebel**,** *Pressure Swing. Adsorption***;** VCH Publishers**:** New York**,** 1994**.**

45. L. Czepirski, J**.** Jagiello**,** *Chem. Eng. Sci***.,** 1989**, 44,** 797-801..

46. J. Jagiello, T. J. Bandosz, K. Putyera, and J. A. Schwarz *J. Chem. Eng. Data*, 1995, **40**, 1288-1292.

47. F.-X. Coudert, M. Jeffroy, A. H. Fuchs, A. Boutin and C. Mellot-Draznieks, *J. Am. Chem. Soc.*, 2008, **130**, 14294–14302..

48. A. L. Myers, J. M. Prausnitz, *AIChE J.*, 1965, **11**, 121-127.

49. J. M. Simmons, H. Wu, W. Zhou and T. Yildirim, *Energy & Environmental Science*, 2011, **4**, 2177.

50. A. J. Arvai, C. Nielsen, *ADSC Quantum-210 ADX Program*, Area Detector System Corporation; Poway, CA, USA, 1983.

51. Z. Otwinowski, W. Minor, in *Methods in Enzymology*, ed. Carter, Jr., C. W.; Sweet, R. M.Academic Press, New York, 1997, vol. **276**, part A, p. 307.

52. G. M. Sheldrick, *Acta Crystallogr,* 2008, **A64**, 112 - 122.

53. G. M. Sheldrick, *SHELEX97*, Program for the crystal structure refinement; University of Göttingen: Göttingen, Germany, 1997.

54. G. M. Sheldrick, *Acta Crystallogr. A*, 1990, **46**, 467 – 473.

55. The software package is available online at http://www.r-project.org.

56. *MATLAB*, The MathWorks Inc., Natick, Massachusetts, 2004.

57. R. L. G. Bordeau, G. Metge, C. Fiorini-Debuisschert, F. Charra and M.-P. Teulate-Fichou, 2008, 130, *J. Am. Chem. Soc.*, 2008, **130**, 16836–16837.

58. H. J. Park, D. W. Lim, W. S. Yang, T. R. Oh, and M. P. Suh, *Chem.-Eur. J.*, 2011, **17**, 7251-7260.

59. E. Y. Lee, S. Y. Jang, and M. P. Suh, *J. Am. Chem. Soc.*, 2005, **127**, 6374-6381.

60. H. K. Chae, J. Kim, O. D. Friedrichs, M. O'Keeffe, and O. M. Yaghi, *Angew. Chem., Int. Ed.*, 2003, **42**, 3907-3909.

61. A. L. Spek, *PLATON99*, Utrecht University: Utrecht, The Netherlands, 1999.

62. S. Yang, X. Lin, A. J. Blake, K. M. Thomas, P. Hubberstey, N. R. Champness, and M**.** Schröder, *Chem. Commun*., 2008, **46**, 6108-6110

63. M. H. Alkordi, and M. Eddaoudi, *"Zeolitelike Metal–Organic Frameworks (ZMOFs): Design, Structure, and Properties." Supramolecular Chemistry: From Molecules to Nanomaterials*, John Wiley & Sons, Ltd., 2012.

64. A. Demessence, D. M. D'Alessandro, M. L. Foo, and J. R. Long, *J. Am. Chem. Soc.*, 2009, **131**, 8784–8786.

65. A. J. Kresge, P. H. Fitzgerald, Y. J. Chiang, *J. Am. Chem. Soc.* 1974, **96**, 4698.

7. Appendix

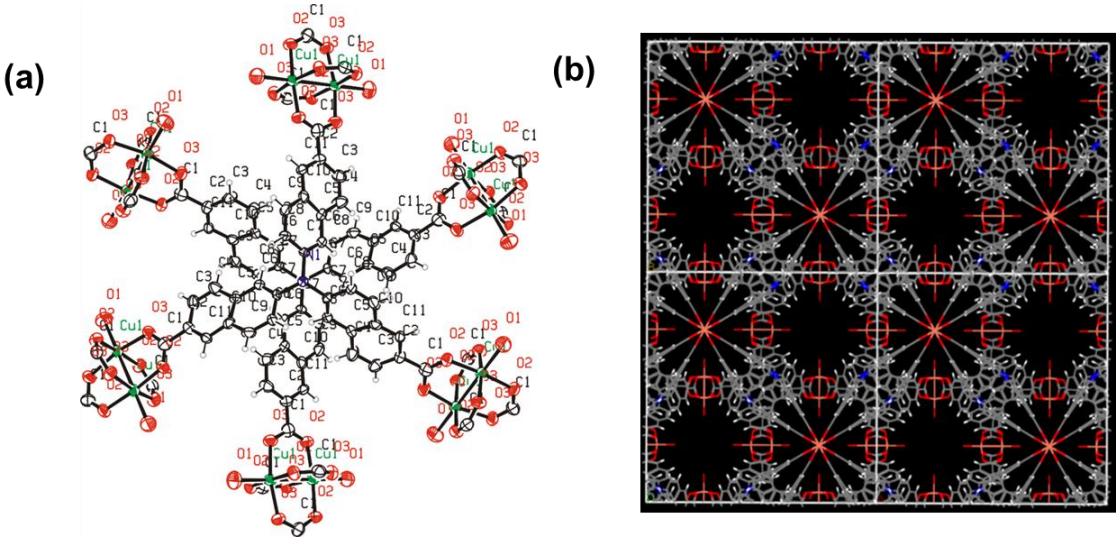

Figure A1. (a) Crystal structure with secondary building units of $[Cu_3NTN_2]\bullet 3H_2O$. (b) X-Ray crystal structure of $[Cu_3NTN_2]\bullet 3H_2O$ seen on the ab plane, color code, C : gray, H : white, O : red, Cu : orange, N : blue.

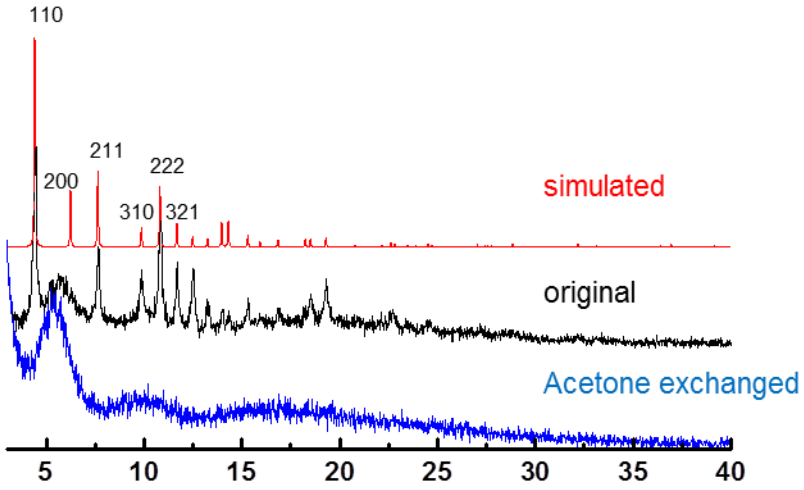

Figure A2. The PXRD patterns of (a) simulated pattern based on single crystal X-ray data of $[Cu_3NTN_2]\cdot 3H_2O$ (red), (b) as-synthesized $[Cu_3NTN_2]\cdot 3H_2O$ (black), (c) acetone exchanged $[Cu_3NTN_2]\cdot$[solvent] (blue)**.**

Table A1. gas adsorption properties of $[Cu_3NTN_2]\cdot 3H_2O$

Gas	*T* / K	*P* / atm	Adsorption capacity (cc g^{-1})
			$[Cu_3NTN_2]$
N_2	77	0.95	334
H_2	77	1	112
	87	1	80.5
CO_2	195	1	209
	298	1	36.4
CH_4	195	1	58.8

국문 초록

새로운 다공성 금속-유기 골격체의 합성과 이산화탄소 포집에의 응용연구

동일한 금속 염과, 유기 리간드를 가지고 다른 용매계에서 수행한 수열반응을 통해 구조가 다른 두 개의 삼차원 다공성 금속-유기 골격체, $[Zn_4O(NTN)_2]\cdot 11DMA\cdot 2H_2O$ (**SNU-150**) 와, $[Zn_5(NTN)_4(DEF)_2][NH_2(C_2H_5)_2]_2\cdot 8DEF\cdot 6H_2O$ (**SNU-151**) 를 합성하였다. **SNU-150** 구조체는 전체적으로 중성인 반면, **SNU-151** 구조체는 수열반응시 diethylformaldehyde 가 첨가된 acetic acid 의 촉매작용으로 인해 부분적으로 분해되어 생성된 diethylammonium 양이온을 동공 내에 포함하고 있는 구조체로 음전하로 하전 되어있다. 두 금속-유기 골격체를 단결정 X-ray 회절을 이용하여 구조를 분석하였다. 가스 흡착 실험을 진행하기 위해 동공 내에 존재하는 용매를 초임계상태의 이산화탄소 건조방법을 이용하여 제거하고 이 때 얻어지는 구조체는 각각 $[Zn_4O(NTN)_2]$ (**SNU-150'**) 와 $[Zn_5(NTN)_4][NH_2(C_2H_5)_2]_2$ (**SNU-151'**) 이다. 분말 X-ray 회절을 통하여 용매가 제거된 구조체의 안정성을 보면, **SNU-150'** 은 일정한 결정성을 유지하는 반면, **SNU-151'**은 부분적으로 무너지는 경향을 보인다. 탈용매화 된 두 구조체로 기체 흡착실험을 한 결과 질소 흡착을 통하여 계산한 동공 크기는 **SNU-150'** 와 **SNU-151'** 이 각각 6.18 Å, 그리고 6.08 Å 으로 차이가 크지 않으나, 231 K 이상의 온도에서의 기체 흡착량과 흡착열 모두 음전하를 띠고 있는 **SNU-151'**이 중성인 **SNU-150'**에 비해 높게 나타났다. 이는 기체분자와 중성

구조체가 상호작용하는 상황에서보다 기체 분자와 dimethylammonium 양이온을 포함하고 있는 음전하의 구조체 사이에서 더 강하게 상호작용하는 것을 보여준다.

주요어 : 다공성 금속-유기 골격체 • 이산화탄소 흡착 • 음전하로 하전된 구조체 • 흡착열 • 선택성